

Quantitative Evaluation of Metal Artifact Reduction Techniques
in MRI

Shannon Heather Kolind

B. Sc. (Physics and Astronomy) University of Victoria, 2001

A THESIS SUBMITTED IN PARTIAL FULFILLMENT OF
THE REQUIREMENTS FOR THE DEGREE OF
MASTER OF SCIENCE

in

THE FACULTY OF GRADUATE STUDIES
DEPARTMENT OF PHYSICS AND ASTRONOMY

We accept this thesis as conforming
to the required standard

THE UNIVERSITY OF BRITISH COLUMBIA

August 2003

© Shannon Heather Kolind 2003

In presenting this thesis in partial fulfilment of the requirements for an advanced degree at the University of British Columbia, I agree that the Library shall make it freely available for reference and study. I further agree that permission for extensive copying of this thesis for scholarly purposes may be granted by the head of my department or by his or her representatives. It is understood that copying or publication of this thesis for financial gain shall not be allowed without my written permission.

Department of Physics and Astronomy

The University of British Columbia
Vancouver, Canada

Date August 29th, 2003

Abstract

Several techniques for metal artifact reduction in MRI were studied in order to determine their effectiveness. The noise and blur introduced by the techniques were also investigated. To this end, non-metallic replicas of two metal implants (stainless steel and titanium/chromium-cobalt femoral prostheses) were fabricated from wax, and MR images were obtained of each component immersed in water. The difference between the images of each metal prosthesis and its wax replica was measured in terms of energy. The difference energy attributed to noise and blur were isolated, resulting in a measure of the metal artifact. This new "gold standard" method was successfully demonstrated to provide a quantitative means of measuring metal artifact.

Several pulse sequences were evaluated in terms of metal artifact reduction capability, as well as signal-to-noise ratio and blur. The analysis revealed that increasing the image bandwidth from ± 16 kHz to ± 64 kHz reduced metal artifact by an average of 60%, while employing View Angle Tilting (VAT) was only slightly more efficient, reducing metal artifact by an average of 63%. The metal artifact reduction sequence (MARS), which combines the increased image bandwidth with VAT as well as an increased slice-select bandwidth, resulted in the least amount of image distortion, reducing the artifact by an average of 79%. The signal-to-noise ratio was lower for MARS, but blurring was found to be significantly improved.

Table of Contents

ABSTRACT.....	ii
TABLE OF CONTENTS	iii
LIST OF FIGURES	vi
GLOSSARY.....	viii
ACKNOWLEDGEMENTS	ix
1 INTRODUCTION.....	1
1.1 CLINICAL USE OF MRI	1
1.2 METAL ARTIFACT.....	1
1.3 PREVIOUS STUDIES IN METAL ARTIFACT USING MRI.....	3
1.4 MOTIVATION	4
1.5 OVERVIEW OF THESIS.....	5
2 NMR THEORY AND BASICS OF MRI.....	6
2.1 NMR PHYSICS.....	6
2.1.1 <i>The Atomic Nucleus</i>	6
2.1.2 <i>Precession in a Magnetic Field</i>	8
2.2 DETECTION OF AN NMR SIGNAL.....	13
2.3 SPIN-ECHOES	18
2.4 SPATIAL LOCALIZATION	20
2.4.1 <i>Slice-Selection</i>	20
2.4.2 <i>Frequency-Encoding</i>	21
2.4.3 <i>Phase-Encoding</i>	22
2.5 MRI PULSE SEQUENCES	24
2.5.1 <i>Gradient-Echo</i>	25
2.5.2 <i>Spin-Echo</i>	25

2.6	SIGNAL-TO-NOISE RATIO	26
3	METAL ARTIFACT	29
3.1	IMAGE ARTIFACTS	29
3.2	OFF-RESONANCE ARTIFACT	29
3.3	OFF-RESONANCE ARTIFACT REDUCTION TECHNIQUES	30
3.4	VIEW ANGLE TILTING	33
3.5	Z-OFFSET	34
4	MATERIALS AND METHODS.....	37
4.1	INTRODUCTION	37
4.2	PHANTOM DESIGN AND CONSTRUCTION.....	37
4.3	MRI PULSE SEQUENCES AND IMAGING PARAMETERS	38
4.4	ANALYSIS	41
4.4.1	<i>Theory</i>	41
4.4.2	<i>Implementation</i>	46
5	RESULTS.....	47
5.1	INTRODUCTION	47
5.2	QUALITATIVE RESULTS - IMAGES	49
5.3	QUANTITATIVE RESULTS - ENERGY	55
5.3.1	<i>Metal Artifact</i>	55
5.3.1.1	<i>Total Difference Energy</i>	56
5.3.1.2	<i>Noise Energy</i>	57
5.3.1.3	<i>Artifact Energy</i>	58
5.3.2	<i>Blur</i>	60
5.3.2.1	<i>Total Difference Energy</i>	61
5.3.2.2	<i>Noise Energy</i>	62
5.3.2.3	<i>Total Artifact Energy</i>	63
5.3.2.4	<i>Blur Energy</i>	64
6	CONCLUSIONS.....	66
6.1	QUANTITATIVE ANALYSIS OF METAL ARTIFACT	66

6.2 . METAL ARTIFACT REDUCTION 66
6.3 BLUR 66
6.4 FUTURE WORK 67
BIBLIOGRAPHY..... 68

List of Figures

Figure 1.1: Metal Artifact in Spine.....	2
Figure 1.2: Chemical Shift Artifact in Shoulder.....	3
Figure 2.1: Semi-Classical Hydrogen Nucleus.....	7
Figure 2.2: Zeeman Energy Splitting.....	9
Figure 2.3: Polarization of Spins	10
Figure 2.4: Precession of Magnetic Moment.....	11
Figure 2.5: Magnetization Vector in Time	14
Figure 2.6: Motion of Magnetization Vector in Rotating Reference Frame.....	15
Figure 2.7: Rotation of Magnetization Vector through Angle α	16
Figure 2.8: Dephasing of Spins with Time Constant T_2^*	17
Figure 2.9: Phase Diagram for CP Spin-Echo Pulse Sequence	19
Figure 2.10: Phase Diagram for a CPMG Spin-Echo Pulse Sequence.....	19
Figure 2.11: Induction Signals as a Train of Spin-Echoes.....	19
Figure 2.12: Negative Lobe of Slice-Select Gradient.....	21
Figure 2.13: Gradient-Echo Pulse Sequence Using Frequency-Encoding	23
Figure 2.14: Three-Step Phase-Encoding	23
Figure 2.15: Gradient-Echo Pulse Sequence Timing Diagram.....	25
Figure 2.16: Multi-Echo CPMG Spin-Echo Pulse Sequence Timing Diagram.....	26
Figure 3.1: Intuitive explanation of VAT	33
Figure 3.2: Oblique k-Space Sampling.....	34
Figure 3.3: Illustration of Z-Offset Theory – No VAT applied.....	35
Figure 3.4: Illustration of Z-Offset Theory – VAT applied.....	36
Figure 4.1: Metal and Wax Prostheses	39
Figure 4.2: Timing Diagram for CSE Pulse Sequence Using VAT	40
Figure 5.1: Qualitative Results – Steel Prosthesis	50
Figure 5.2: Qualitative Results – Wax Replica of Steel Prosthesis	51
Figure 5.3: Qualitative Results – Titanium Prosthesis.....	52
Figure 5.4: Qualitative Results – Wax Replica of Titanium Prosthesis	53
Figure 5.5: Qualitative Results – Picker International Phantom.....	54

Figure 5.6: Qualitative Results – ROI used in Picker International Phantom	55
Figure 5.7: Total Energy for Various Metal Artifact Reduction Techniques	56
Figure 5.8: Noise Contribution to Total Energy	58
Figure 5.9: Artifact Energy	59
Figure 5.10: Total Energy for Blur Study	61
Figure 5.11: Noise Energy for Blur Study	62
Figure 5.12: Total Artifact Energy for Blur Study	63
Figure 5.13: Blur Energy for Artifact Reduction Techniques Involving VAT	64

Glossary

2DFT	Two-Dimensional Fourier Transform
BW	Bandwidth
CNS	Central Nervous System
CP	Carr-Purcell
CPMG	Carr-Purcell-Meiboom-Gill
CSE	Conventional Spin-Echo
CT	Computed Tomography
EPI	Echo-Planar Imaging
FDA	Food and Drug Administration
FFT	Fast Fourier Transform
FID	Free Induction Decay
FSE	Fast-Spin-Echo
FT	Fourier Transform
GE	Gradient-Echo
^1H	Hydrogen Nucleus; Proton
IFT	Inverse Fourier Transform
MARS	Metal Artifact Reduction Sequence
MRI	Magnetic Resonance Imaging
NMR	Nuclear Magnetic Resonance
RF	Radio Frequency
ROI	Region of Interest
SNR	Signal-to-Noise Ratio
T_1	Spin-Lattice Relaxation Time
T_2	Spin-Spin Relaxation Time
TE	Echo-Time
TR	Repetition Time
VAT	View Angle Tilting
Voxel	Volume Element

Acknowledgements

This work could not have been done without the support of many people.

Alex MacKay has been a wonderful supervisor, providing guidance and support, as well as making me feel welcome and comfortable in the group. I look very forward to continuing to work with him.

Qing-San Xiang has also been amazingly helpful, answering my every question with tremendous attention and detail.

The rest of the MRI research group, Corree Laule, Thor Bjarnason, Charmaine Chia, Elana Brief, Sumia Tahir, Burkhard Maedler, Irene Vavasour, Craig Jones, and Ken Whittall, have made me feel at home, and have been incredibly helpful. Thanks for making this experience so enjoyable that I don't want to leave!

Thanks also to the MRI technologists, who have not only been patient with my mistakes, but have taught me to use the MRI scanner confidently, and made it fun.

I've also been very lucky to have the support of the staff and members of the physics department at UBC, notably Janet Johnson, Janis McKenna, Tony Walters, Lydia Wong, Dave Axen, and Fran Bates, who've looked out for me in terms of scholarships, teaching assistant positions, mid-semester crises, etc. I would also like to thank George Beer, Andy Sachrajda, Mike Hayden and Charles Picciotto for helping me to get the funding for this project and the next.

I never would have been here in the first place without the love and encouragement of Karl and Debbie Kolind, whom I am very lucky to know and love both as parents and as people. The same goes for my sister and brother, Chelsea Kleckner and Kristopher Kolind, who are friends first and siblings second. I've also relied heavily on the support of my extended and widespread but still very close family, the Blythes, Kolinds, Laframboises, Loves, McCallums, Mooneys, Stackhouses, and Yeats.

Last but not most of all, a million thanks to Richard Stackhouse for his unbelievable support, love, and friendship. Thank you for always being there for me, and making every day exciting.

This work was done with the support of an NSERC PGS-A. I am very grateful to NSERC for providing me with this funding, and continuing to support my research.

1 Introduction

1.1 Clinical Use of MRI

The development of diagnostic imaging began in the early 1900s after x-rays were discovered. In the 1950s nuclear medicine was introduced, using gamma cameras to detect radiation signals originating from low-level radioactive chemicals injected into the body. When digital imaging techniques were introduced in the 1970s, Computed Tomography (CT) became widely used in hospitals all over the world, and is still one of the most important diagnostic tools in use today. However, in the early 1980s, Magnetic Resonance Imaging (MRI) was approved for commercial, clinical use by the Food and Drug Administration (FDA), and it quickly caught the attention of clinicians due to its ability to detect abnormalities in the spine, brain stem and cerebellum. CT, using x-rays, is ineffective in this area due to the bony structures present, while MRI, using magnetism, has no such limitation. Initially, MRI was used to complement CT scans of the Central Nervous System (CNS), and was barely used in other regions of the body, due to issues such as long imaging times and associated motion artifact. In the mid 1980s many of these issues were resolved, and it was soon realized that while CT is superior for imaging bone or hard tissue, MRI produces much more detailed images of soft tissue. MRI is also a more powerful tool, allowing the contrast to be changed, which causes different types of tissue to be highlighted. The imaging plane can also be easily altered without moving the patient. Finally, MRI involves no radiation and has no known harmful effects. It is currently estimated that over 20 million MR exams are performed each year in the United States alone.

1.2 Metal Artifact

A severe limitation of magnetic resonance imaging (MRI) is its sensitivity to the presence of metal. MRI uses a uniform static magnetic field to induce the signal used to create an image, and magnetic field gradients to spatially locate the origin of the generated signal. Even small perturbations to the magnetic field can upset the imaging process and the clinical image can be rendered meaningless. In the presence of metal, the local magnetic field is distorted, which leads to mis-mapping or even loss of signal. Spatial localization depends on a consistent magnetic field gradient being applied across the object or region to be imaged,

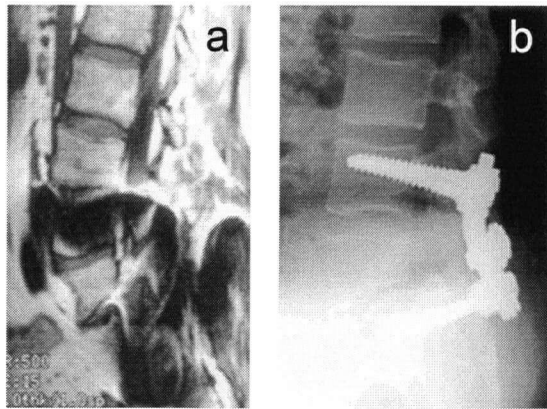


Figure 1.1: Metal Artifact in Spine

(a) A sagittal MR image shows geometric distortion around a posterior fixation device in the spine. (b) A lateral radiograph shows the posterior fixation device. (Reproduced with permission from Peter Munk and the Radiological Society of North America [1]).

producing a regular gradation of magnetic field strength, allowing the assignment of a particular signal to a specific point in space. Tissue bordering metal objects becomes influenced by the induced magnetic field of the object in addition to the applied magnetic field, leading to misallocation of the signal. This can distort the image such that the clinical information present is no longer useful. Thus while MRI is routinely used pre-operatively to diagnose and plan surgery for patients with orthopedic disorders, it has limited worth in post-operative assessment of metal implants, which would be invaluable for determining the status of the prosthesis and the response of the body. It is especially desirable to monitor the health of the soft tissue adjacent to any orthopedic hardware. This geometric distortion is illustrated in the sagittal MR image of the spine of a 39-year-old man with a posterior fixation device, seen in Figure 1.1a [1]. For comparison, the posterior fixation device can be seen in the lateral radiograph in Figure 1.1b.

Problems with metal artifact are not limited to imaging metal prostheses. The presence of metal can distort the magnetic field for a significant distance, so even imaging other regions of a patient with any metal in or on their body can result in image distortion. This could potentially lead to false positive or false negative results in patient exams.

The magnetic field can also be disturbed by metallic surgical instruments, which are used in interventional MRI. This is especially of concern in the case of guided stereotactic surgery, a minimally invasive method of performing neurosurgery by creating only a small opening in

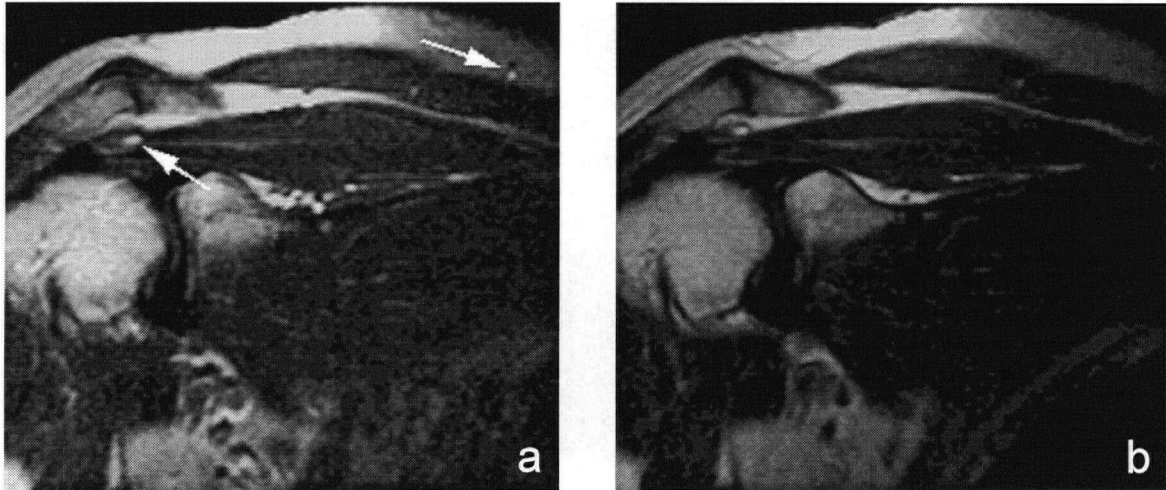


Figure 1.2: Chemical Shift Artifact in Shoulder

MR image of the shoulder demonstrating chemical shift artifact. (a) features no chemical shift artifact correction, and the arrows indicate the presence of chemical shift artifact. (b) has been corrected for chemical shift artifact. (Reproduced with permission from Wayne Patola [3]).

the skull and directing a thin straight probe to a precise target or structure in the brain using a three-dimensional imaging method such as MRI. Precise geometrical accuracy is required, so image distortions are particularly detrimental.

Susceptibility artifacts are also caused by any difference in magnetic susceptibility between objects, including fat and water, or water and air. The natural difference in magnetic susceptibility between most biological tissues and air is of the order of 10 ppm, which is sufficient to cause a significant distortion and loss of signal at the boundary [2], and is referred to as chemical shift artifact. This becomes apparent by comparing Figure 1.2a, an image of the shoulder without correction for chemical shift artifact, to Figure 1.2b, which has less chemical shift artifact [3]. In the top right corner, as indicated by the arrow, the fluid in the vessel is seen in the correct location but the fat around it has been shifted upwards in the image producing a hole which should be around the vessel.

1.3 Previous Studies in Metal Artifact using MRI

Due to the frequent need to image patients with metal present in their body, much research has been done to reduce the effects of metal artifact. Although there have been many reports on imaging patients with metal implants [4, 5, 6], no definitive method has been universally adopted for artifact reduction. Several techniques are commonly used to diminish the

severity of metal susceptibility artifact, many of which are described by Eustace et al. [7]. These include choosing a prosthesis made of a material with low magnetic susceptibility, setting the frequency-encoding direction along the long axis of the metal component, using a short echo-time (TE), and choosing a spin-echo pulse sequence.

A clever technique still not in common usage is View Angle Tilting (VAT) [8], which has been demonstrated to be clinically useful for reducing the distortion in images when imaging patients with metal implants [1, 9, 10] and during interventional Fast-Spin-Echo (FSE) MRI where inserted needles distort the local magnetic field [11]. VAT results in a marked reduction in the severity of the metal susceptibility artifact, and can be employed without increasing the imaging time. Unfortunately, it introduces blurring, and only reduces the artifact in one direction. These deficiencies are lessened in the Metal Artifact Reduction Sequence (MARS), which involves VAT and increased bandwidths. MARS also has shortcomings, including a decreased signal-to-noise ratio (SNR).

1.4 Motivation

While many metal susceptibility artifact reduction techniques have been suggested, none have been shown to be sufficient, or are used universally. Without a quantitative evaluation of these techniques and combinations of them, it is difficult to determine the most effective approach.

Also, each method has drawbacks that can mask its ability to reduce metal artifact, and it is necessary to measure the disadvantages as well as the advantages of each approach in order to establish its overall performance. For example, some techniques may successfully reduce metal artifact, but introduce additional noise or blurring.

In order to make a quantitative measurement of the metal susceptibility artifact, it must be known how the undistorted image would appear if it were free of metal artifact. Without a standard against which to measure the efficiency of a technique, most studies have been limited to qualitative comparisons.

In this work, such a “gold standard” was obtained by creating a replica of a metal phantom out of wax, which has the advantages of being non-metallic and having a similar susceptibility to water. The difference between MR images of the metal phantom and of the wax replica was measured, and resolved into contributions from noise, metal artifact, and

blur using energy relationships. While an image artifact is defined as any feature appearing in the image that does not exist in the imaged object, this study focused on metal susceptibility artifact, so treated noise and blur separately. The goal was to compare the effectiveness of various metal artifact reduction techniques in terms of metal artifact reduction, noise, and blur.

Of particular interest was MARS, which was developed by Dr Qing-San Xiang and Dr Alex MacKay at the University of British Columbia. MARS combines VAT with increased bandwidths to further improve metal artifact in both the frequency-encoding direction and the slice-select direction, while reducing the blurring intrinsic to VAT. While this technique has been examined in previous studies [1, 9, 10, 12], the “gold standard” approach allows measurements of the metal artifact, noise and blur to be obtained and compared to VAT and other techniques.

1.5 Overview of Thesis

A brief background for MRI physics is presented in chapter 2, including the basics of NMR, and the spatial localization techniques used for MRI. Chapter 3 deals with image artifact, specifically metal artifact and techniques commonly used to reduce it. In chapter 4, the methods and materials are described for the experiments executed in order to quantify metal artifact, blur and noise. This includes the phantom fabrication, the pulse sequences and parameters used, and the analysis theory and implementation. In chapter 5, both qualitative and quantitative results are presented and discussed. Finally, conclusions and future experiments are put forward in chapter 6.

2 NMR Theory and Basics of MRI

2.1 NMR Physics

In 1944, I.I. Rabi was awarded the Nobel Prize in Physics for experiments he and his colleagues performed six years earlier that led to a measurement of the nuclear magnetic moment [13, 14]. This was considered the first nuclear magnetic resonance (NMR) experiment, but NMR was not achieved in condensed matter until 1946. Felix Bloch and Edward Purcell shared the Nobel Prize in Physics in 1952 for this achievement; they conducted their experiments independently and used different methods [15, 16, 17]. Bloch's method, induction, currently dominates the NMR field. Physical and chemical properties of a sample can be determined from its NMR signal, which can be obtained non-invasively, but using traditional NMR, sample size is limited because the signal is summed over the entire sample.

The mathematics of NMR imaging were introduced by R.R. Ernst and W.A. Anderson in 1966 [18] based on the Fourier transform, and improved with computer technology and the fast Fourier transform (Ernst was awarded the 1991 Nobel Prize in Chemistry for his contribution to NMR). P.C. Lauterbur put these principles into action in 1973 and was one of the first to obtain NMR images [19]. When NMR imaging became widely used clinically, the N was dropped due to the negative connotations of the word nuclear, and NMR imaging became known as MRI.

2.1.1 The Atomic Nucleus

The nucleus of an atom contains protons and neutrons, collectively called nucleons. Electrons occupy orbitals outside of the nucleus, and the orbitals are filled in an order strictly dictated by quantum mechanics. The electrons fill the lowest energy state, or orbital, available, but the Pauli Exclusion Principle states that no two fermions (such as electrons, protons or neutrons) can occupy the same energy state. Thus the orbitals are filled in an order of ascending energy. Nucleons occupy nuclear orbits that are filled according to corresponding rules to filling electron orbitals. A minimum energy arrangement occurs when the orbital angular momentum and the spin angular moment sum to zero. This leads to a

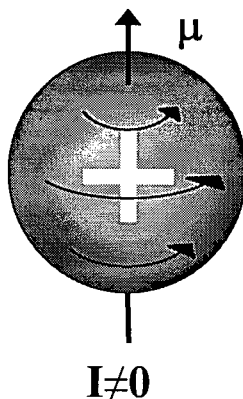


Figure 2.1: Semi-Classical Hydrogen Nucleus

A hydrogen nucleus can be considered semi-classically to be a single proton with non-zero spin leading to an angular momentum I and a magnetic moment μ . The moving charge induces μ , which forms an electric current loop.

pairing force, dictating that each of a pair of nucleons occupy orbitals that cancel each other's angular momentum.

Semi-classically, the nucleus can be considered to be a sphere with an electric charge distribution dictated by the presence of the nucleons. If the total angular momentum of the nucleus is not zero, the sphere will spin and a magnetic moment will be induced by the moving charge which forms an electric current loop. NMR relies upon the magnetic dipole moment, so only nuclei with non-zero total angular momentum will contribute to the NMR signal.

Quantum mechanically, the nucleons can be labeled with the quantum numbers j , ℓ , and s , representing the total angular momentum, the orbital angular momentum and the spin angular momentum, respectively. The coupling of the nucleons is such that in a given state, the total angular momentum of the nucleus is given by the vector sum of the angular momentum of each individual nucleon. The total angular momentum of the nucleus is called the nuclear spin, I . The magnetic dipole moment, μ , is directly proportional to I , with a constant of proportionality γ , the gyromagnetic ratio, so

$$\mu = \gamma I. \quad (2.1)$$

This is illustrated in Figure 2.1. As can be seen in Equation (2.1), if the nuclear spin is zero, the magnetic dipole moment will also be zero. The balance between the number of protons and neutrons determines the angular momentum in the nucleus. Since paired nucleons have

zero net angular momentum, they do not contribute to the magnetic dipole moment of the nucleus. Unpaired neutrons, protons, or both, result in non-zero net spin and therefore a non-zero net magnetic dipole moment. Thus the electromagnetic properties of the atom are determined by only a few valence nucleons [20].

The most commonly imaged nucleus is hydrogen, ^1H , because it is so abundant in the human body. Approximately 60% of the body is composed of water, and ^1H is also present in fat, so all together nearly 66% of the atoms in the human body are hydrogen [21, 22]. The hydrogen nucleus contains only one nucleon, a proton. Since the proton is a fermion, its spin angular momentum quantum number $s = \pm 1/2$. Its projection onto the z-axis then has the possible values $m_s = -s, -s+1, \dots, +s$, which in this case turn out to be $m_s = \pm 1/2$. In the ground state of ^1H , $m_s = +1/2$, and since there is only one nucleon, $\ell = 0$, so $I = \ell + s = 1/2$. Thus hydrogen has a non-zero spin and a non-zero magnetic dipole moment and so exhibits NMR.

2.1.2 Precession in a Magnetic Field

When placed in an external magnetic field, \mathbf{B} , a nucleus with a magnetic moment $\boldsymbol{\mu}$ will interact with energy

$$E = -\boldsymbol{\mu} \cdot \mathbf{B}. \quad (2.2)$$

If the direction of \mathbf{B} is chosen to be along the z-axis, $\mathbf{B} = B\hat{\mathbf{z}}$, so we are only interested in μ_z . Since there is only one nucleon for a hydrogen nucleus, $I = j$, so μ_z is equal to γj_z , and j_z is the projection onto the z-axis. $j_z = \hbar s$, since $\ell = 0$ for a sole nucleon. Thus

$$E = -\mu_z B = -\gamma j_z B = -\gamma \hbar s B. \quad (2.3)$$

Since s can be $\pm 1/2$ for a fermion, there are two possible values for the energy which correspond to two different orientations. The spin-up orientation has $s = +1/2$, and therefore $E^- = -\gamma \hbar B / 2$, and the spin-down orientation has $s = -1/2$, and therefore the higher energy of $E^+ = \gamma \hbar B / 2$. The difference in energy between the two states is $\Delta E = \gamma \hbar B$. This is called Zeeman energy splitting, and is illustrated in Figure 2.2.

The probability of a proton occupying one of the two energy states is given by a Boltzmann distribution:

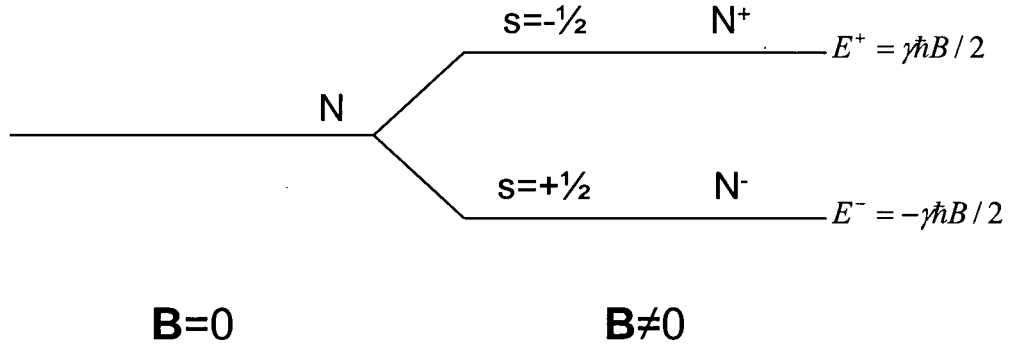


Figure 2.2: Zeeman Energy Splitting

Zeeman energy splitting caused by the presence of an external magnetic field. For a large number N of protons, N^+ will have $s=-1/2$, and N^- will have $s=1/2$, leading to corresponding energies E^+ and E^- . The probability of a particular proton having either energy is given by a Boltzmann distribution.

$$P(E) = Ce^{-E/kT} \quad (2.4)$$

where C is a constant of the system, k is the Boltzmann constant and T is the temperature in Kelvin. For a large number of protons, the ratio of protons in the spin-up energy state to those in the spin-down energy state is

$$R = N^- / N^+ = P(E^-) / P(E^+) = e^{\Delta E/kT} = e^{\gamma\hbar B/kT}. \quad (2.5)$$

At an average room temperature of 300K, and a magnetic field of 1.5T, $\Delta E/kT \approx 1.02 \times 10^{-5}$, so $R \approx 1.0000102$. This means that there are a very few (about 1 in 10^5) more protons in the spin-up state than in the spin-down state. This leads to a net macroscopic magnetization M_0 equal to the total magnetic moment per unit volume given by

$$\begin{aligned} M_0 &= \mu(N^- - N^+) = \mu(N^- + N^+) \frac{(N^- - N^+)}{(N^- + N^+)} \\ &= \mu N \frac{(R-1)}{(R+1)} = \mu N \frac{(e^{\Delta E/kT} - 1)}{(e^{\Delta E/kT} + 1)} = \mu N \tanh(\Delta E/2kT) \end{aligned} \quad (2.6)$$

where N is the total number of protons. For very small $\Delta E/2kT$, $\tanh(\Delta E/2kT) \approx \Delta E/2kT$, so

$$M_0 \approx \mu N \Delta E/2kT = N\mu^2 B/kT = N\gamma^2 \hbar^2 B/4kT. \quad (2.7)$$

M_0 is referred to as the thermal equilibrium value of the magnetization. The polarization of a group of spins is illustrated in Figure 2.3. M_0 is proportional to the external magnetic field, the total number of protons, and the inverse of temperature. The

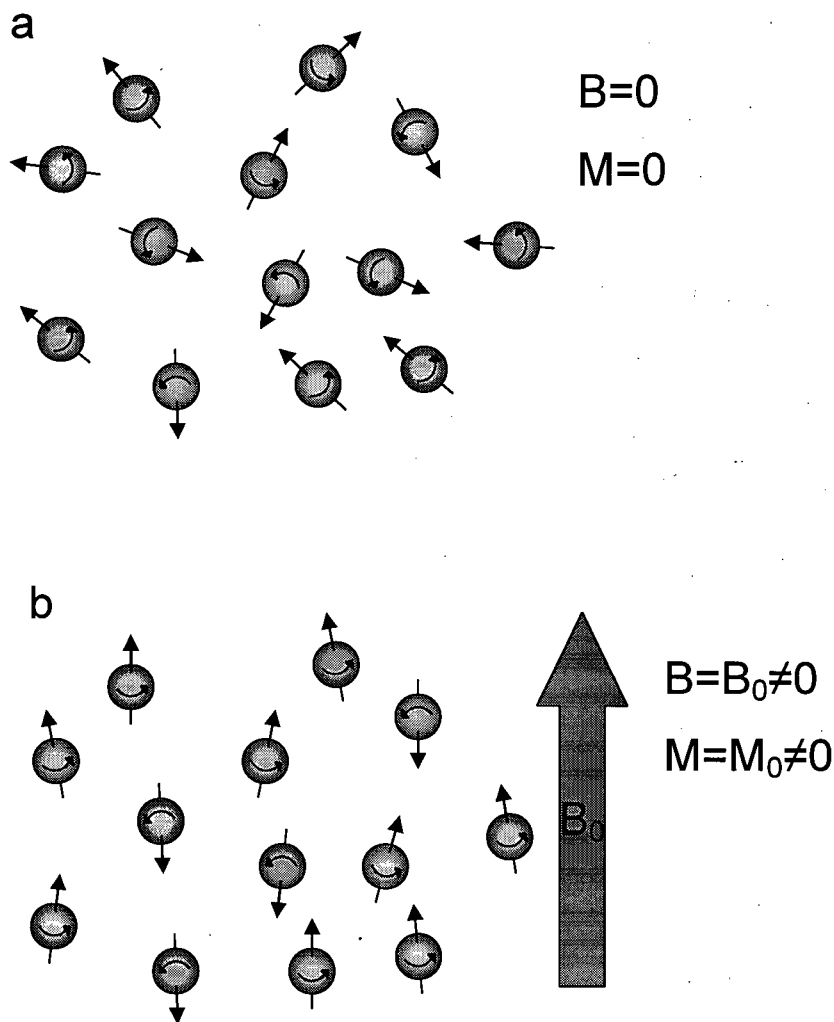


Figure 2.3: Polarization of Spins

A group of spins begins with random orientations (a), but when an external magnetic field is applied (b), they are polarized such that the thermal equilibrium magnetic moment M_0 is parallel to the angular momentum and the magnetic field B_0 .

NMR signal is proportional to the magnetic moment, so for a high signal-to-noise ratio it is desirable to have a large sample, a high magnetic field, and a low temperature. In practice, these elements are limited by complications such as cost, artifact, and biological factors.

Now that the equilibrium magnetization has been established, the equation of motion of this vector can be determined. In 1897, Joseph Larmor found that if an aligning force is applied to a spinning object, it will undergo precession. So if a spinning object is tipped away from the aligning force, it will precess about the axis of the force. Using classical mechanics, the rate of change of the angular momentum is equal to the torque (\mathbf{T}):

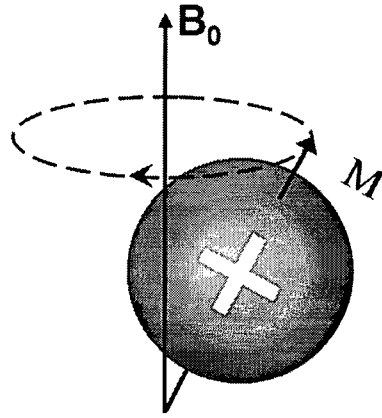


Figure 2.4: Precession of Magnetic Moment

The motion of the magnetic moment M is analogous to a spinning top or pendulum, except with a magnetic field (B_0) acting as an aligning force instead of a gravitational field.

$$\frac{d\mathbf{I}}{dt} = \mathbf{T}. \quad (2.8)$$

From electrodynamics, the torque is related to the magnetic moment and the magnetic field:

$$\mathbf{T} = \mathbf{M} \times \mathbf{B}, \quad (2.9)$$

and since $\mathbf{M} = \gamma\mathbf{I}$,

$$\frac{d\mathbf{M}}{dt} = \gamma\mathbf{M} \times \mathbf{B}. \quad (2.10)$$

This relationship holds true regardless of whether or not the magnetic field is time dependent [23]. It indicates that the magnetic moment precesses after being tipped away from the direction of the magnetic field, with the change in magnetic moment perpendicular to both the magnetic moment and the magnetic field. The angular frequency of precession is referred to as the Larmor frequency, $\omega_0 = -\gamma B$. The precession is illustrated in Figure 2.4.

The equation of motion can also be calculated using quantum mechanical arguments. The observable μ has the equation of motion:

$$\frac{d\langle\mu\rangle}{dt} = \frac{i}{\hbar} \langle [H, \mu] \rangle = \frac{i}{\hbar} \langle H\mu - \mu H \rangle \quad (2.11)$$

where H is the Hamiltonian. Then $H = -\boldsymbol{\mu} \cdot \mathbf{B}$, so

$$\frac{d\langle\boldsymbol{\mu}\rangle}{dt} = \frac{i}{h}\langle(-\boldsymbol{\mu}\cdot\mathbf{B})\boldsymbol{\mu} - \boldsymbol{\mu}(-\boldsymbol{\mu}\cdot\mathbf{B})\rangle \quad (2.12)$$

but $\boldsymbol{\mu} = \gamma\mathbf{j}$, and by the commutation properties of angular momentum operators, $\mathbf{j}\times\mathbf{j} = ih\mathbf{j}$, so

$$\frac{d\langle\boldsymbol{\mu}\rangle}{dt} = -\gamma^2\langle\mathbf{B}\times\mathbf{j}\rangle = \gamma\langle\boldsymbol{\mu}\rangle\times\mathbf{B}. \quad (2.13)$$

Since the total magnetic moment per unit volume is $\mathbf{M} = N\langle\boldsymbol{\mu}\rangle$, this becomes

$$\frac{d\mathbf{M}}{dt} = \gamma\mathbf{M}\times\mathbf{B} \quad (2.14)$$

which is identical to Equation (2.10).

Since the quantum mechanical approach yielded exactly the same results as the semi-classical approach, the following sections can simply use a semi-classical approach.

Equation (2.14) describes the motion of the magnetic moment in a magnetic field assuming that there are no other interfering factors. Bloch [15, 16] proposed a more detailed phenomenological relationship which is widely used today:

$$\frac{d\mathbf{M}}{dt} = \gamma\mathbf{M}\times\mathbf{B} - \frac{M_x\hat{\mathbf{x}} + M_y\hat{\mathbf{y}}}{T_2} - \frac{(M_z - M_0)\hat{\mathbf{z}}}{T_1}. \quad (2.15)$$

The additional terms come from relaxation, which is the inclination to return to the equilibrium magnetization \mathbf{M}_0 .

T_1 is called the longitudinal relaxation time since it occurs toward \mathbf{M}_0 along the direction of \mathbf{B} , or the spin-lattice relaxation time because it is a measure of the time it takes for the spins to transfer energy to the lattice, their environment.

T_2 is called the transverse relaxation time since it occurs in directions perpendicular to the direction of \mathbf{B} , or the spin-spin relaxation time because it is a measure of the time it takes for interactions with other spins to cause dephasing, decreasing the net magnetization. Two spins near each other distort the local magnetic field, leading to variations in their precession frequencies such that the average frequency remains the same, but the individual spins' frequencies vary randomly as they move through the sample. T_2 is a measure of the rate at which spins are dephased through spin-spin interactions.

The Bloch equation can be separated into its components along each axis:

$$\begin{aligned}
\frac{dM_x}{dt} &= \gamma M_y B_0 - \frac{M_x}{T_2} \\
\frac{dM_y}{dt} &= -\gamma M_x B_0 - \frac{M_y}{T_2} \\
\frac{dM_z}{dt} &= \frac{M_z - M_0}{T_1}
\end{aligned} \tag{2.16}$$

with the following general solutions:

$$\begin{aligned}
M_x(t) &= [M_x(0)\cos(\omega_0 t) + M_y(0)\sin(\omega_0 t)]e^{-t/T_2} \\
M_y(t) &= [-M_x(0)\sin(\omega_0 t) + M_y(0)\cos(\omega_0 t)]e^{-t/T_2} \\
M_z(t) &= M_0 + [M_z - M_0]e^{-t/T_1},
\end{aligned} \tag{2.17}$$

where $\omega_0 = \gamma B_0$.

A special case common to MRI occurs when $M_x(0) = 0$, $M_y(0) = M_{xy}^0$, $M_z(0) = M_z^0$. Then

Equations (2.17) become:

$$\begin{aligned}
M_x(t) &= M_{xy}^0 \sin(\omega_0 t) e^{-t/T_2} \\
M_y(t) &= M_{xy}^0 \cos(\omega_0 t) e^{-t/T_2} \\
M_z(t) &= M_0 + (M_z^0 - M_0) e^{-t/T_1}.
\end{aligned} \tag{2.18}$$

The time development of each of these three components can be seen in Figure 2.5a. The three-dimensional motion of the magnetization vector is depicted in Figure 2.5b.

Finally, these equations can be simplified by considering only transverse and longitudinal directions to the magnetic field. Then the transverse and longitudinal magnetizations are, respectively,

$$M_T(t) = M_{xy}^0 e^{-t/T_2} e^{i\omega_0 t} \tag{2.19}$$

And

$$M_L(t) = M_0 + (M_z^0 - M_0) e^{-t/T_1}. \tag{2.20}$$

2.2 Detection of an NMR Signal

In MRI, the signal is generated by applying an oscillating magnetic field pulse for a short time, orthogonal to the static magnetic field, \mathbf{B}_0 . The pulse rotates \mathbf{M} away from the

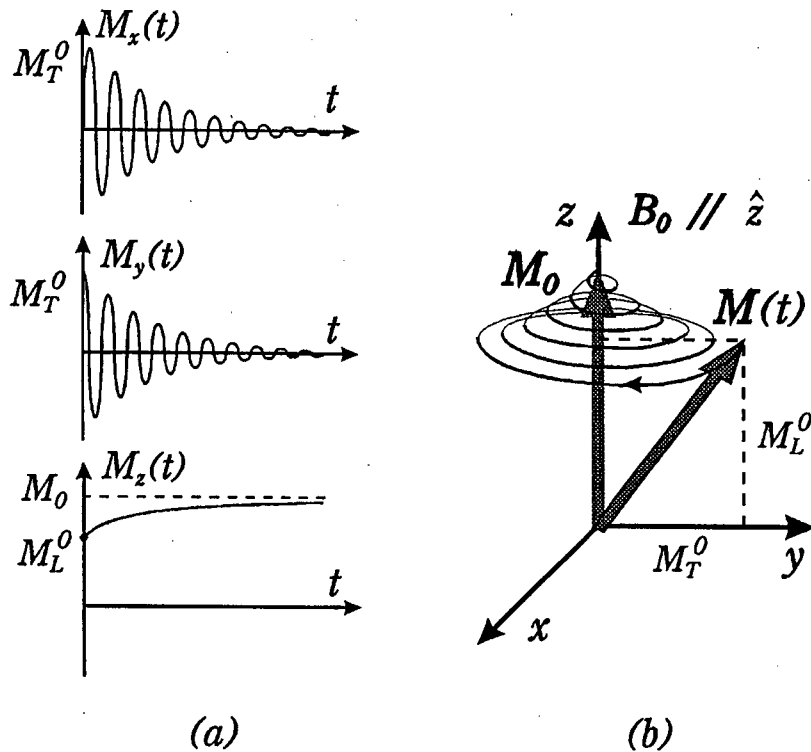


Figure 2.5: Magnetization Vector in Time

(a) The components of the magnetization vector as functions of time. (b) The three-dimensional motion of the magnetization vector. (Reproduced with permission from S. Xiang)

equilibrium position, \mathbf{M}_0 . The magnetic field pulse oscillates at the Larmor frequency, which is the precession frequency of the magnetization vector. The oscillation of the magnetic field is necessary to push the magnetization vector in the same direction at each rotation. For conventional MRI, the Larmor frequency turns out to be in the radio frequency (RF) range, so the pulse is often referred to as the RF pulse. This concept is more transparent when considered in a rotating reference frame. If we use a reference frame that rotates in the same plane and with the same angular frequency as the precessing spin (i.e. the Larmor frequency), then the axis of rotation (the z -axis) remains the same, and the x - and y -axes are translated to the x' - and y' - axes ($z \rightarrow z$, $x \rightarrow x'$, $y \rightarrow y'$). In this new reference frame, the magnetization vector does not rotate, so the only change in \mathbf{M} is caused by relaxation, as illustrated in Figure 2.6. The Larmor frequency for a hydrogen atom in a magnetic field of 1.5T is 63.9 MHz, while T_1 and T_2 are on the order of 3 seconds for pure water, and

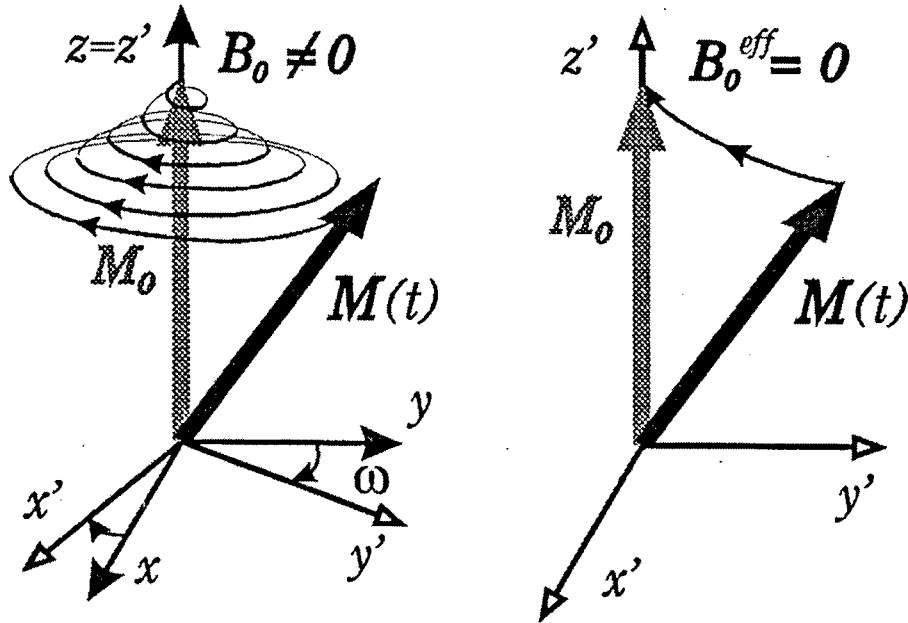


Figure 2.6: Motion of Magnetization Vector in Rotating Reference Frame

On the left, the non-rotating frame of reference results in complicated motion for the magnetization vector, \mathbf{M} . On the right, the rotating reference frame simplifies the motion so that the only movement of \mathbf{M} is due to relaxation. (Reproduced with permission from S. Xiang)

$T_1 \approx 1s$, $T_2 \approx 10-100ms$ for biological tissue, so the effects of relaxation can be neglected during the RF pulse. Then Equation (2.15) can be rewritten (neglecting relaxation) as:

$$\frac{d\mathbf{M}}{dt} = \mathbf{M} \times (\gamma\mathbf{B}_0 + \boldsymbol{\omega}_0) = \mathbf{M} \times \mathbf{B}_{\text{eff}} \quad (2.21)$$

where the effective magnetic field $\mathbf{B}_{\text{eff}} = (\gamma\mathbf{B}_0 + \boldsymbol{\omega}_0)$. Since \mathbf{M} is not rotating in the rotating reference frame, and relaxation is neglected, $\frac{d\mathbf{M}}{dt} = \mathbf{0}$, so $\mathbf{B}_{\text{eff}} = \mathbf{0}$. Thus

$$\boldsymbol{\omega}_0 = -\gamma\mathbf{B}_0. \quad (2.22)$$

If \mathbf{M} is initially along the z -axis, and the RF magnetic field has constant magnitude B_1 and frequency ω_0 , and is applied along the x' direction for a time τ , \mathbf{M} precesses about the x' -axis with angular frequency γB_1 through an angle α given by

$$\alpha = \gamma B_1 \tau, \quad (2.23)$$

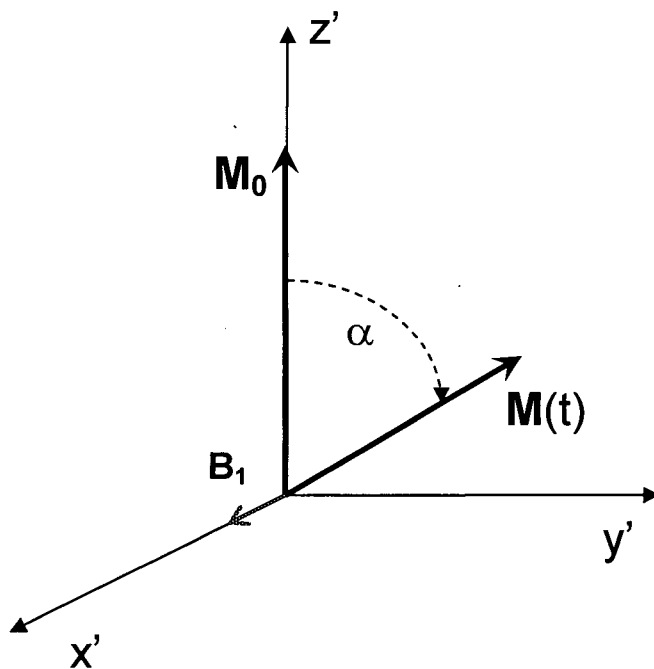


Figure 2.7: Rotation of Magnetization Vector through Angle α
 In the rotating reference frame, the magnetization vector gets rotated about B_1 through angle α away from the z' -axis.

as seen in Figure 2.7. If the RF field is “off-resonance”, i.e. not applied at the Larmor frequency, the force will not be in a consistent direction in the rotating reference frame, and will be much less effective at tilting the magnetization vector.

If α is 90° , \mathbf{M} will be rotated to the y' -axis, so the longitudinal component of \mathbf{M} will be zero. If α is 180° , \mathbf{M} will be along the $-z'$ -axis, so the transverse component of \mathbf{M} will be 0.

By Equations (2.19) and (2.20), M_L approaches M_0 exponentially with a time constant T_1 , and M_T decays exponentially with a time constant T_2 .

According to Faraday’s Law, changes in magnetic flux through a coil of conducting wire caused by time varying magnetic fields induce a current in the coil. If a coil is placed along the x - or y -axis, an induced current will be measured due to the rotating \mathbf{M} . The transverse magnetization decays exponentially, and the corresponding induced signal decay is called a free induction decay (FID).

The same coil used to detect the NMR signal is usually used to transmit the RF excitation pulse. If it is aligned along the y -axis, the excitation will be along the y -axis, and can be considered to occur at time $t = 0$. At $t = 0^+$, the transverse magnetization \mathbf{M}_T is along the $-x$ -

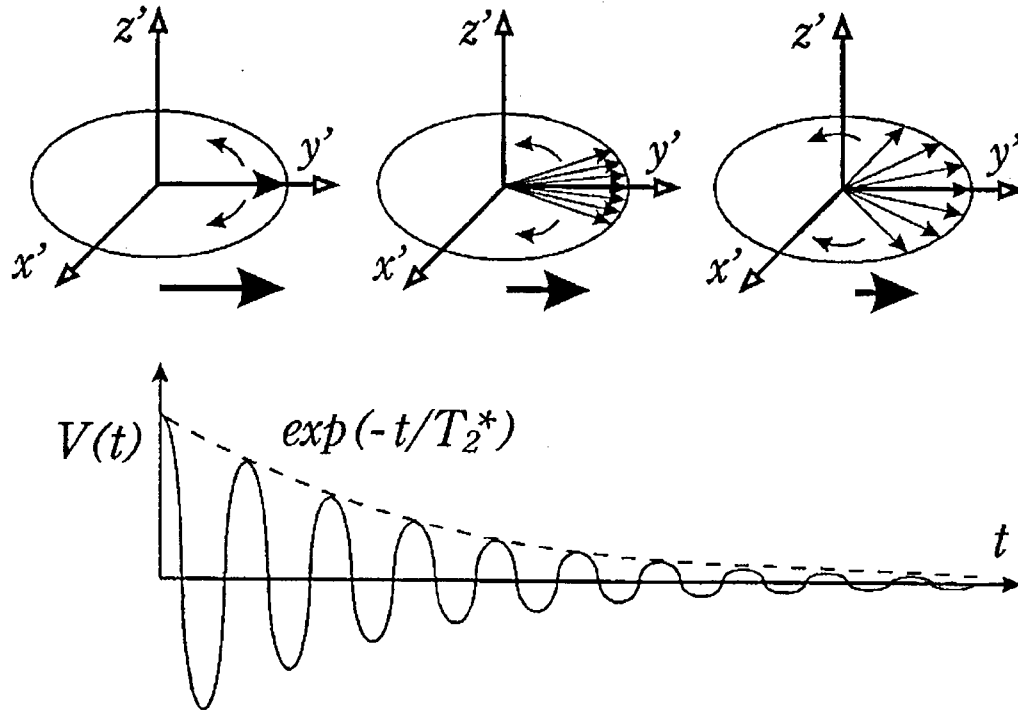


Figure 2.8: Dephasing of Spins with Time Constant T_2^*

In the rotating reference frame, as the spins dephase due to magnetic field inhomogeneities, the signal decays exponentially with a time constant T_2^ . (reproduced with permission from S. Xiang)*

axis, so there is no signal detected. At time $t = \frac{\pi}{4\omega_0}$, \mathbf{M}_T is along the y-axis, generating a signal. At time $t = \frac{\pi}{2\omega_0}$, \mathbf{M}_T is along the x-axis, so again there is no signal. At $t = \frac{3\pi}{4\omega_0}$, the transverse magnetization is along the $-y$ -axis, so the signal has the opposite sign to that at $t = \frac{\pi}{4\omega_0}$. The time varying signal is sinusoidal, decaying with a time constant T_2^* (pronounced “tee two star”) due to spin-spin interactions (characterized by time constant T_2) as well as inhomogeneities in the static magnetic field. T_2^* is shorter than T_2 since there are more causes of dephasing, and is given by

$$\frac{1}{T_2^*} = \frac{1}{T_2} + \gamma\Delta B, \quad (2.24)$$

where ΔB is a measure of the field inhomogeneity. This process is illustrated in Figure 2.8.

2.3 Spin-echoes

In 1950, Hahn [24] applied an RF pulse to a sample following the FID, producing a second FID. He used a 90° pulse a time τ after an initial 90° pulse, but it is more intuitive to consider a 90° pulse followed by a 180° pulse. Such a refocusing pulse was used by Carr and Purcell in 1954 [25].

In the rotating reference frame, if \mathbf{M}_0 is initially along the z-axis and is rotated 90° about the x' -axis, it will then lie along the y' -axis. In the rotating frame, there is no precession, but dephasing due to spin-spin interactions and field inhomogeneities begins immediately. The net magnitude of \mathbf{M} decreases along the y' -axis as the phases are spread into a fan-shaped distribution. After a time τ , a 180° pulse is applied about the x' -axis, rotating all of the spins by 180° so that the same fan shaped distribution appears about the $-y'$ -axis. The spins continue to precess with the same frequency as before the 180° pulse since only the phase was altered by the pulse. The dephasing becomes refocusing, so that at time $t = 2\tau$ the spins are all in phase again along the $-y'$ -axis, producing a large FID signal called a spin-echo. This sequence is called the CP sequence for Carr and Purcell, and is often denoted $90^\circ x' - \tau - 180^\circ x' - \tau$ -echo. The phase relation of the spins is depicted in Figure 2.9.

A further modification was introduced by Meiboom and Gill producing the CPMG sequence [26], denoted $90^\circ x' - \tau - 180^\circ y' - \tau$ -echo. In this case, the 180° pulse is applied along the y' axis, so that the echo takes place along the y' -axis instead of the $-y'$ -axis, as seen in Figure 2.10. The CP sequence depends on having a very accurate 180° pulse, or else the spins will not line up along the $-y'$ -axis but have some component in the z-direction when the echo occurs, reducing the magnitude of \mathbf{M}_T . The CPMG sequence is more forgiving; if the pulse does not rotate the spins through exactly 180° , they will still rephrase toward the y' -axis away from the longitudinal direction, maintaining the magnitude of \mathbf{M}_T . When several refocusing pulses are applied in a row (producing a train of echoes), the errors in the CP sequence will accumulate, while in the CPMG sequence, they will counteract each other.

When a single RF pulse is applied, the FID will decay with time constant T_2^* due to spin-spin interactions and field inhomogeneities. By applying 180° refocusing pulses every 2τ , a train of echoes is produced with the peak of each echo smaller in amplitude than the last due to T_2 relaxation, not T_2^* , since the effects of the inhomogeneities are handled by the refocusing. Thus the envelope formed by the peak amplitudes of the FIDs will decrease exponentially

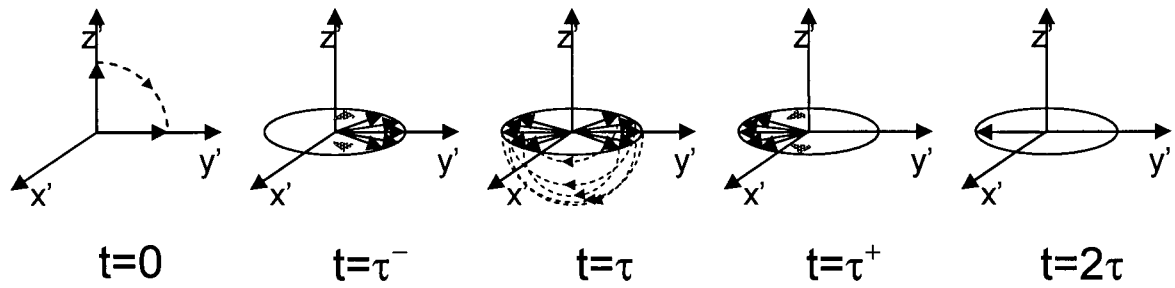


Figure 2.9: Phase Diagram for CP Spin-Echo Pulse Sequence

If a 90° pulse occurs about the x' -axis at time 0, and a 180° pulse about the x' -axis occurs at time τ , an echo will occur at time 2τ .

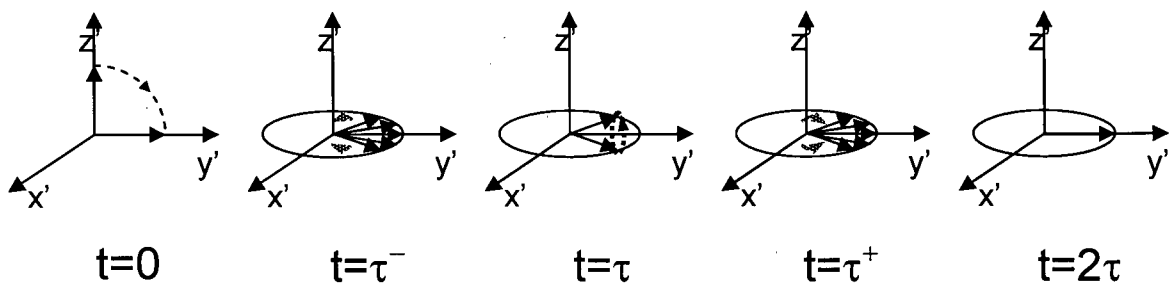


Figure 2.10: Phase Diagram for a CPMG Spin-Echo Pulse Sequence

If a 90° pulse occurs about the x' -axis at time 0, and a 180° pulse occurs about the y' -axis at time τ , an echo will occur at time 2τ .

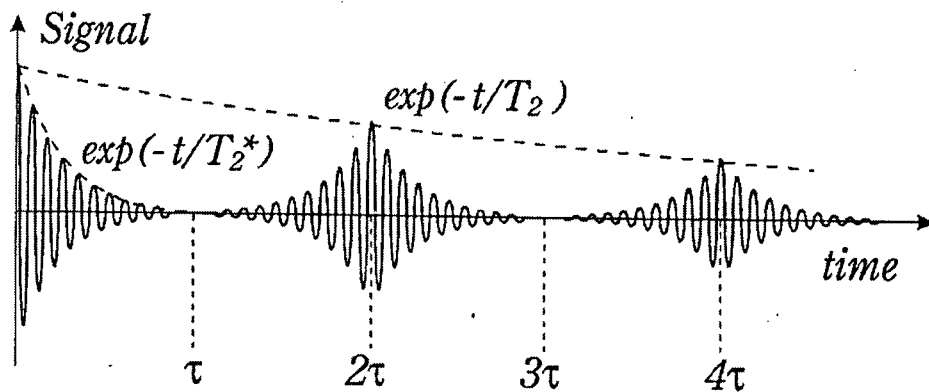


Figure 2.11: Induction Signals as a Train of Spin-Echoes

Each echo decays exponentially with a time constant of T_2^* due to magnetic field inhomogeneities, while the peaks of the echoes decay exponentially with a time constant of T_2 due to spin-spin interactions. (Reproduced with permission from S. Xiang)

with a time constant T_2 , while each echo decays with time constant T_2^* , as seen in Figure 2.11. The signal intensity at the peaks can be found as follows:

$$S(2n\tau) = S(0)e^{-2n\tau/T_2} \quad (2.25)$$

where $S(t)$ is the signal intensity at time t , and n is a non-negative integer.

2.4 Spatial Localization

In order to create an image, it is necessary to know where the protons from which each portion of the NMR signal arises are spatially located. This is accomplished by superimposing a magnetic field gradient on the static magnetic field \mathbf{B}_0 . These gradients are very small compared to \mathbf{B}_0 ; \mathbf{B}_0 is typically 1.5T, while the gradients are usually a maximum of 20 - 30 mT/m. Gradients can be applied along all three orthogonal axes, with a separate set of coils for each direction. The magnetic field perturbation can then be written as follows:

$$\Delta\mathbf{B} = \mathbf{r} \cdot \mathbf{G} = xG_x + yG_y + zG_z. \quad (2.26)$$

The gradients generally cause a linear change in the magnetic field across the sample. The change in magnetic field creates a linear change in the Larmor frequency of the spins located at different points in the sample.

There are three main techniques for spatial localization: slice-selection, frequency-encoding, and phase-encoding. Any of the techniques can be applied in any physical direction, but for simplicity, the logical convention of applying slice-selection along the z-axis, frequency-encoding along the x-axis, and phase-encoding along the y-axis, will be followed.

2.4.1 Slice-Selection

A single slice with a finite thickness can be isolated parallel to the xy-plane using a gradient along the z-axis. With the magnetic field gradient applied, the Larmor frequencies of the spins will change linearly along the z-direction. If a 90° RF pulse is applied with a given frequency, it will only fully rotate the spins with a Larmor frequency matching the frequency of the pulse. All of these spins will be at the same z location, and so will create a plane orthogonal to the z-axis. The selected frequency is given by:

$$\omega = \gamma(B_0 + \mathbf{r} \cdot \mathbf{G}) = \gamma(B_0 + zG_z). \quad (2.27)$$

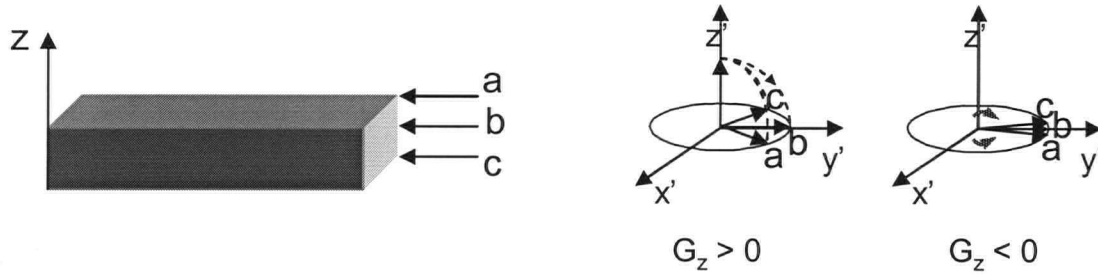


Figure 2.12: Negative Lobe of Slice-Select Gradient

After the RF pulse, spins at different points along the z-axis (a,b,c) are tipped along different directions since they have different Larmor frequencies, and then are refocused by the negative lobe of the slice-select gradient.

To obtain a particular slice thickness, a frequency band $\Delta\omega$ must be selected instead of a single frequency. This cannot be accomplished using a fixed amplitude RF pulse in the rotating frame. Instead, the amplitude is varied in time. To a first order approximation, the temporal modulation of the amplitude of the RF pulse is related by Fourier transform to its frequency spectrum. Thus a Gaussian time dependence will result in a Gaussian frequency spectrum, or a Sinc shaped RF pulse will produce a rectangular frequency spectrum, and hence a rectangular slice. The slice thickness is given by:

$$d = \frac{\Delta\omega}{\gamma G} \quad (2.28)$$

Within the slice, since the spins do not all have the same Larmor frequency, they get tipped into the transverse plane along different paths, and so are not in phase after the rotation. This can be remedied by applying a negative gradient lobe immediately after the slice-select gradient to refocus, as demonstrated in Figure 2.12.

2.4.2 Frequency-Encoding

Following the application of the slice-selection, a gradient can be applied in the x-direction such that spins in different positions along the x-axis precess at different Larmor frequencies. Using quadrature signal detection, both real and imaginary signals are collected and combined to give a complex signal. Ignoring the effects of relaxation, the induction signal is given by:

$$c(t) = \int dx P(x) e^{i\gamma G x t} \quad (2.29)$$

where $c(t)$ is the time dependent complex signal, $P(x)$ is a one-dimensional projection of the transverse magnetization along the x-direction, and γxG is the Larmor frequency in the rotating reference frame. When multiplied by time, this expression describes the angle made by the precessing spin in time t in the rotating frame, or the phase. Recalling that a forward Fourier Transform (FT) can be defined as:

$$f(k) = \frac{1}{\sqrt{2\pi}} \int_{-\infty}^{\infty} dx F(x) e^{ixk}, \quad (2.30)$$

and the corresponding inverse Fourier Transform (IFT) can be defined as:

$$F(x) = \frac{1}{\sqrt{2\pi}} \int_{-\infty}^{\infty} dk f(k) e^{-ixk}, \quad (2.31)$$

then the complex signal can be rewritten as:

$$S(k) = \int_{-\infty}^{\infty} dx P(x) e^{ixk} \quad (2.32)$$

where $S(k)$ is the complex signal, and $k = \gamma Gt$. Since the signal is a function of k , it is said to reside in k -space. The one-dimensional projection of the transverse magnetization can then be recovered using an IFT:

$$P(x) = \frac{1}{2\pi} \int_{-\infty}^{\infty} dk S(k) e^{-ixk}, \quad (2.33)$$

where k is known and S is measured. Thus the one-dimensional projection $P(x)$ of the spatially distributed magnetization can be recovered by applying an IFT to the complex signal.

For the IFT, k must run from negative infinity to infinity. One way of approximating this is to apply a negative gradient lobe just before acquisition, allowing sampling of negative k -space. Thus if the total time of application of the gradient is T , k_{\max} will be γGT , and since the signal is very small for $\pm k_{\max}$, the integral is well approximated. This is called a gradient-echo, and the pulse sequence is shown in Figure 2.13.

2.4.3 Phase-Encoding

Phase can be used to spatially encode the third dimension, but it requires multiple steps. At each step, the slice-selection is performed, followed by the application of the phase-encoding gradient along the y-axis for a fixed time T , and finally the frequency-encoding and data

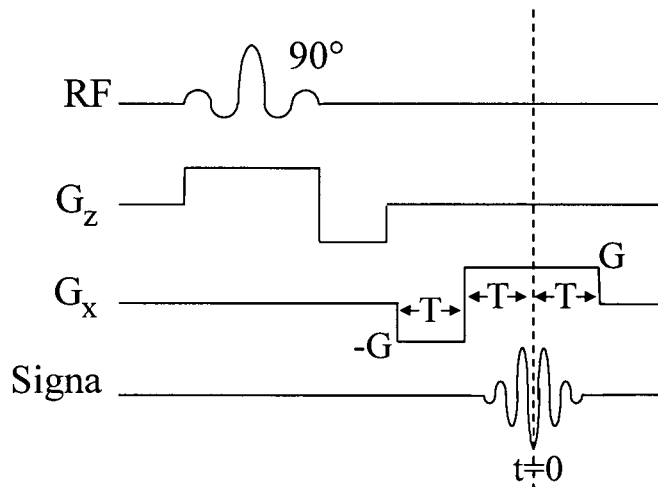


Figure 2.13: Gradient-Echo Pulse Sequence Using Frequency-Encoding

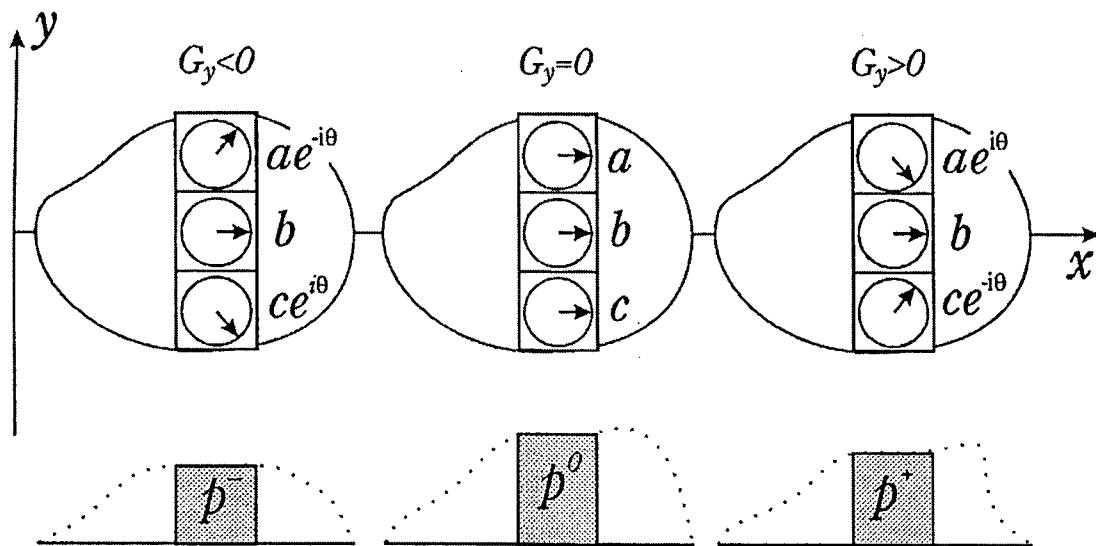


Figure 2.14: Three-Step Phase-Encoding

Different gradients are applied along the y-axis: one negative, one zero, and one positive. Each results in a different projection obtained by frequency-encoding due to the phases of the magnetizations a, b and c. (reproduced with permission from S. Xiang)

acquisition. The amplitude of G_y is incremented at each step in order to impose different phases on the spins for each step.

For example, in order to spatially encode three voxels in known locations in a column parallel to the y-axis, three steps can be applied with $G_y = -g$, $G_y = 0$, and $G_y = g$, where g is a

positive constant. If each voxel has a magnetization a , b , or c respectively, the one-dimensional projections onto the x-axis will be given by:

$$p^- = ae^{-i\gamma gT} + b + ce^{i\gamma gT} \quad (2.34)$$

$$p^0 = a + b + c \quad (2.35)$$

$$p^+ = ae^{i\gamma gT} + b + ce^{-i\gamma gT} \quad (2.36)$$

for each gradient applied, respectively, as illustrated in Figure 2.14. The projections are known from the results of the frequency-encoding, so the equations can be solved for a , b and c .

The equations can be put in matrix form:

$$m = \begin{pmatrix} a \\ b \\ c \end{pmatrix} \quad (2.37)$$

$$p = \begin{pmatrix} p^- \\ p^0 \\ p^+ \end{pmatrix} \quad (2.38)$$

$$F = \begin{bmatrix} e^{-i\gamma gT} & 1 & e^{i\gamma gT} \\ 1 & 1 & 1 \\ e^{i\gamma gT} & 1 & e^{-i\gamma gT} \end{bmatrix} \quad (2.39)$$

$$p = Fm \quad (2.40)$$

$$m = F^{-1}p. \quad (2.41)$$

In general, a fast Fourier Transforms (FFT) is used to analyze the data, which requires that the number of projections must be a power of two. Since a resolution of much greater than three voxels is usually required, it is common to use 64, 128, 256 or 512 steps. For 256 steps, F will be a 256x256 matrix.

2.5 MRI Pulse Sequences

Although there are many pulse sequences in common usage in MRI to suit different applications, the discussion in this section will be limited to two common pulse sequences: a gradient-echo (GE) two-dimensional Fourier Transform (2DFT), and a conventional spin-echo (CSE) 2DFT.

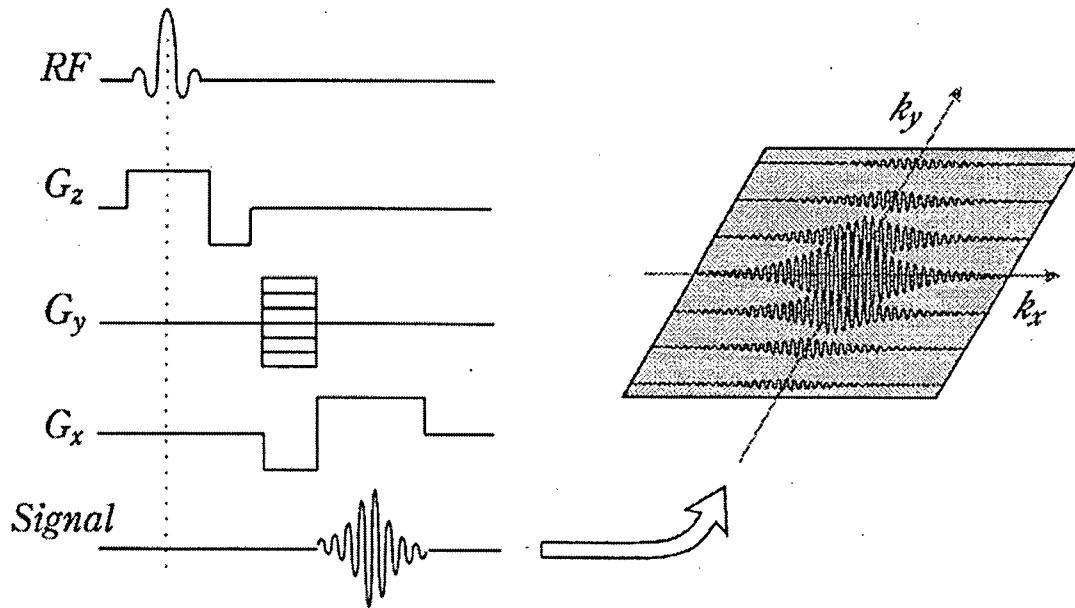


Figure 2.15: Gradient-Echo Pulse Sequence Timing Diagram

A gradient-echo pulse sequence with slice-selection, phase-encoding and frequency-encoding. The induction signals, depicted as 2D raw data in k -space, are on the right. Each horizontal line is produced from one phase-encoding step. (Reproduced with permission from S. Xiang)

2.5.1 Gradient-Echo

The timing diagram in Figure 2.15 illustrates the GE pulse sequence. The RF pulse and G_z are applied simultaneously to select the slice, and slice-selection is followed by a negative G_z lobe to rephase the spins. The area under the rephaser is half the area under the slice-select gradient. The multiple phase-encoding steps are represented by the various amplitudes for G_y . The negative G_x lobe preceding the frequency-encoding gradient allows negative k -space to be sampled, and creates the echo during frequency-encoding.

2.5.2 Spin-Echo

The timing diagram for the CSE pulse sequence is seen in Figure 2.16. Using a spin-echo will result in more signal due to better rephasing, and is less prone to artifact.

The diagram shown is a multi-echo sequence, with two echoes depicted. TE is the time from the center of the 90° pulse to the center of the echo. The time between successive echoes is referred to as the echo spacing.

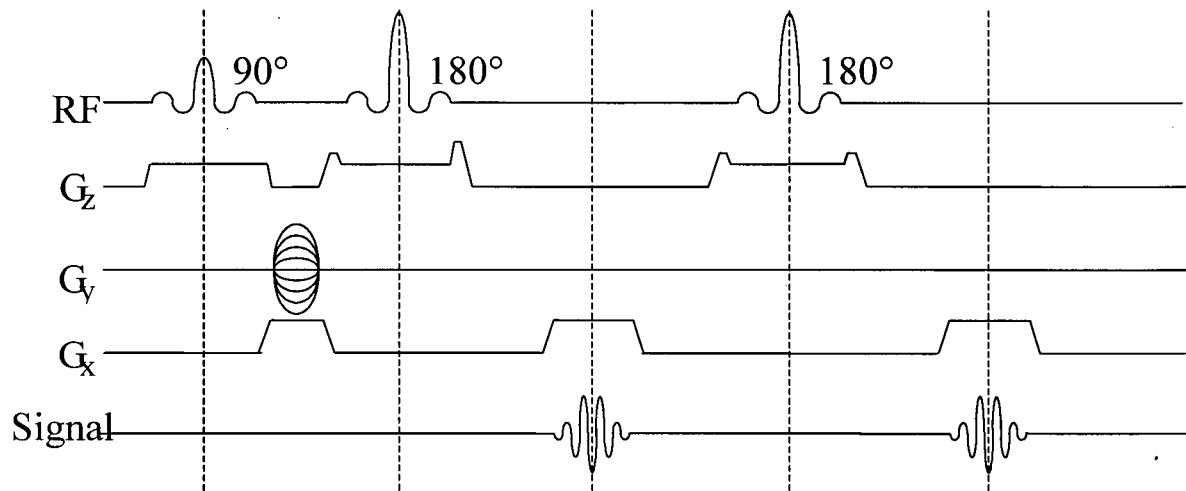


Figure 2.16: Multi-Echo CPMG Spin-Echo Pulse Sequence Timing Diagram

The shape of the phase-encoding gradient is a sinusoid to minimize quantization error which occurs because the size of the step may not be exactly as prescribed due to limited resolution. The negative refocusing lobe for the slice-select gradient following the RF excitation is not present, but has been replaced with extra lobes on each side of the 180° pulses. As long as the area under the z-gradient between the center of the 90° pulse and the data acquisition is zero, the spins will be in phase. Note that the area changes sign mid-way through the 180° pulse. The lobes on the 180° pulses also serve to destroy signal corruption from magnetization generated by flaws in the 180° pulses, and are called crushers.

The shapes of the gradients are more realistic than in the timing diagram of the GE pulse sequence. Time is required (typically on the order of 1ms) to ramp the gradients up to their desired amplitude, resulting in a trapezoidal shape.

The dephaser for the frequency-encoding gradient appears before the 180° pulse, which is more time efficient, allowing for shorter TE's. The frequency-encoding gradient is also called the READ gradient because it is applied during data acquisition.

The sequence is repeated for different phase-encoding steps.

2.6 Signal-to-noise Ratio

Although there are many ways of measuring and reporting the noise present in an MR image, the signal-to-noise ratio (SNR) is often defined as

$$SNR = \frac{Intensity}{\sigma}, \quad (2.42)$$

where σ is the standard deviation of the noise. Typically, the noise is white, and the intensity changes from voxel to voxel, so a mean intensity value is taken over a region of interest (ROI) expected to produce uniform signal and divided by the standard deviation of those same voxel values to give the SNR. Since the data has both imaginary and real components, the magnitude image is often used for analysis and display, but the noise is distributed differently when superimposed on signal than where there is no significant signal [27]. Gaussian noise with a zero-mean is expected to assume both positive and negative values, but when taking the magnitude, all of the values where there is no signal will become positive, with a Rayleigh distribution. Where superimposed on signal which is much larger than the amplitude of the noise, the noise will remain normally distributed.

The intensity is proportional to the local transverse magnetization, and the size of the sample:

$$Intensity \propto M\Delta x\Delta y\Delta z. \quad (2.43)$$

The variance of the noise after image reconstruction can be shown to be

$$\sigma^2 = \frac{p \cdot BW}{N} \quad (2.44)$$

where p is the total noise power (a constant of the system), N is the total number of samples in the data acquisition, and BW is the bandwidth of the RF receiver,

$$BW = \gamma \cdot FOV \cdot G \quad (2.45)$$

where FOV is the field of view.

Using the dependencies of the signal intensity and σ , it can be determined what factors will affect the SNR. Increasing the main magnetic field B_0 increases the magnetization, and also increases the induction signal, so the SNR is roughly proportional to $B_0^{1.2}$. Decreasing the coil size decreases p because noise comes from the entire volume of the coil, and so increases the SNR. Increasing TR and decreasing TE allows for more recovery of the longitudinal magnetization and less decay of the transverse magnetization, respectively, and therefore increases the SNR. Increasing the slice thickness increases Δz , which increases the signal and hence the SNR. Collecting the data multiple times and averaging the signal decreases the noise, so for white noise, SNR is proportional to the square-root of the number of averages. The noise is proportional to the square-root of the BW , so the SNR is proportional

to $BW^{-1/2}$. Increasing the FOV increases the number of spins per voxel in both the x- and y-directions, so SNR is proportional to FOV^2 . Increasing the resolution or matrix size in the y-direction increases the number of samples but decreases Δy , so overall the SNR is proportional to $(y\text{-matrix-size})^{-1/2}$. In the x-direction, N_x and Δx are affected the same way as for y, but in general N_x/BW is kept constant, so the net effect is that the SNR is inversely proportional to the x-matrix size.

3 Metal Artifact

3.1 Image Artifacts

Image artifacts are generally defined as any feature appearing in the image that does not exist in the imaged object. These artifacts can be subdivided into many different categories, including motion artifact caused by movement of the subject, aliasing artifact caused by under-sampling, and truncation artifact caused by not sampling high spatial frequencies, among many others. Off-resonance artifacts, or geometric distortion artifacts, were the general class of artifact investigated in this study.

3.2 Off-Resonance Artifact

In MRI, image reconstruction relies on properly spatially encoded NMR signals. The NMR signals are encoded using various magnetic fields. A constant, uniform magnetic field, B_0 , polarizes the spins so that they precess at the Larmor frequency, which is proportional to B_0 . Linear gradient fields are applied along three axes at various times in order to alter the Larmor frequency such that the frequency and phase of the NMR signal generated by a given spin determines its spatial position. If a spin does not have the expected frequency and phase prescribed, it will be mapped to the wrong location.

Off-resonance artifacts occur when there are modifications to the desired local Larmor frequency. One situation in which this occurs is when the B_0 field is inhomogeneous. This is usually a slowly changing perturbation and so does not cause serious artifacts, and can be corrected by mapping this field before imaging [28]. Another is when more than one type of molecule is being imaged. The electrons of an atom circulate about the direction of B_0 , causing a small magnetic field at the nucleus opposing the externally applied magnetic field. The effective magnetic field (B_{eff}) at the nucleus is therefore less than the applied field.

The precession frequency is given by $\omega = \gamma B$, so protons experiencing different effective magnetic fields will precess at different frequencies. This is called chemical shift (δ), and is measured in ppm relative to a standard:

$$\delta = \frac{(\omega - \omega_{\text{ref}}) \times 10^6}{\omega_{\text{ref}}} \quad (3.1)$$

Magnetic susceptibility effects are also a type of off-resonance artifact. The net magnetic field effect caused by an external field, B , is related to the magnetic field intensity, H , as follows:

$$B = \mu H . \quad (3.2)$$

where μ is the magnetic permeability, or the ability of a particular material to concentrate magnetic fields. The induced magnetic field in the material, M , is given by:

$$M = \chi H , \quad (3.3)$$

where χ is the magnetic susceptibility. χ is also given by:

$$\chi = \mu - 1 . \quad (3.4)$$

χ is therefore a measure of how strongly a material becomes magnetized. A diamagnetic material, which has no unpaired orbital electrons, has a negative χ since B_0 actually induces a weak M in the opposite direction to B_0 , reducing the effective magnetic field. Water and most body tissues are diamagnetic. Paramagnetic materials, such as aluminum, have unpaired orbital electrons, and have a small positive χ since M is in the same direction as B_0 . Ferromagnetic materials have a large positive χ and remain magnetized even after B_0 is removed. Iron, cobalt and nickel are all ferromagnetic.

Differences in magnetic susceptibilities distort the local magnetic field, resulting in different Larmor frequencies than expected. The stronger the difference in χ , the more pronounced the artifact.

3.3 Off-Resonance Artifact Reduction Techniques

Several methods are widely used for reducing the distortion due to off-resonance effects [4, 5, 6, 7]. One way to minimize distortion is to use an MR technique that is less sensitive to these effects. Pulse sequences with refocusing pulses tend to be less vulnerable to dephasing, so a CSE pulse sequence would be a better choice than a GE sequence for off-resonance artifact minimization. With a CSE pulse sequence, the artifact takes the form of a geometric distortion due to voxel mis-mapping along the frequency-encoding (x-) direction. Techniques such as GE have similar distortion, but also suffer from dephasing and hence lose signal. The off-resonance artifact in techniques with non-Cartesian k-space scanning (such

as spiral or radial) exhibits itself as local blurring and noise-like intensities spread across the FOV.

Some factors that can decrease the effects of off-resonance artifacts are a weaker B_0 , a larger frequency-encoding BW, a larger slice-select BW, and decreased resolution along the x-direction. For example, the chemical shift between water and fat is about 3.5 ppm. In a static magnetic field of 1.5 T, the resulting shift in precession frequency is found as follows:

$$\Delta\omega = \gamma_{water} B_0 (3.5 ppm) \quad (3.5)$$

$$\Delta\omega \cong (42.6 MHz / T)(1.5 T)(3.5 \times 10^{-6}) \quad (3.6)$$

$$\Delta\omega \cong 220 Hz . \quad (3.7)$$

So the difference in precessional frequencies between water and fat is about 220 Hz. The effects of the above factors are illustrated as follows.

Weaker B_0 :

If B_0 is 0.5 T, then $\Delta\omega \cong 73$ Hz. This will result in less displacement of the voxels relative to each other. This is not very practical, however, since the static magnetic field of an MRI scanner is not usually alterable, and smaller magnetic fields result in a lower SNR.

Larger frequency-encoding BW:

If the BW is 16 kHz, and the FOV in the READ direction is divided into 256 voxels, each voxel has a bandwidth given by:

$$BW / voxel = 16 kHz / 256 \quad (3.8)$$

$$BW / voxel = 62.5 Hz . \quad (3.9)$$

So a difference in precessional frequencies between water and fat of 220 Hz results in a difference in mapping of $220 Hz / (62.5 Hz/voxel) \cong 3.5$ voxels. So the fat will be mapped 3 or 4 voxels away from where water in the same location is mapped to. If the BW is increased to 64 kHz,

$$BW / voxel = 64 kHz / 256 \quad (3.10)$$

$$BW / voxel = 250 Hz \quad (3.11)$$

$$Voxel\ difference = \frac{220 Hz}{250 Hz / voxel} \quad (3.12)$$

$$\text{Voxel difference} \cong 1\text{voxel} . \quad (3.13)$$

So the fat will only be mis-registered by about 1 voxel instead of 3 or 4. The disadvantage of this is that it results in a lower SNR.

Larger slice-select BW:

The same technique can be applied in the slice-select direction to reduce the shift along the slice-select axis. In the slice, the artifact is distorted slice location and slice thickness. Increasing the slice-select bandwidth decreases the relative difference in Larmor frequencies, decreasing the magnitude of the shift along the slice-select axis, resulting in a less warped slice.

Decreased resolution in the x-direction:

This is similar to increasing the frequency-encoding BW. If the number of frequency points is reduced from 256 to 128, maintaining a BW of 16 kHz, the resulting voxel difference is given by:

$$BW / \text{voxel} = 16\text{kHz} / 128 \quad (3.14)$$

$$BW / \text{voxel} = 125\text{Hz} \quad (3.15)$$

$$\text{Voxel difference} = \frac{220\text{Hz}}{125\text{Hz} / \text{voxel}} \quad (3.16)$$

$$\text{Voxel difference} \cong 2\text{voxels} . \quad (3.17)$$

There are also several techniques for use especially in reducing metal artifact. The frequency-encoding axis should be aligned with the long axis of the metal component because it is the direction in which the field distortions are the most prominent. The long axis of the metal component should also be parallel to the direction of the main field, B_0 , to minimize interactions with the field. Larger RF coils should be used since the tuning of larger coils is less affected by metal, although this also results in a decrease in the SNR. The type of metal also has a large effect on the severity of metal artifact. While the cost, availability and mechanical qualities are the factors traditionally used to select the type of metal used for a prosthesis, the magnetic susceptibility has become another important factor. This is because materials with large magnetic susceptibilities such as stainless steel or cobalt

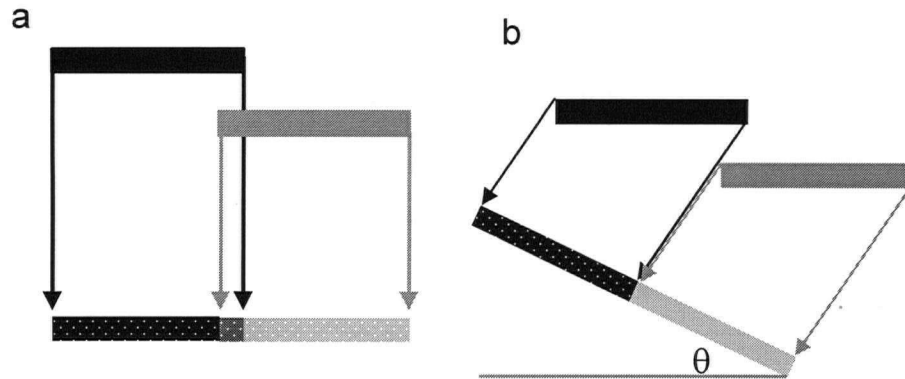


Figure 3.1: Intuitive explanation of VAT

(a) Two pieces of tissue are displaced in the slice-selection and read directions due to chemical shift. The image will contain a pixel shift along the read direction, shown as tissue overlap. (b) When VAT is added, the read direction is tilted away from the horizontal by an angle θ , canceling the displacements in the two directions and resulting in no overlap.

chrome cause more metal artifact than titanium alloys, making titanium the more MR compatible metal.

3.4 View Angle Tilting

A field inhomogeneity correction technique referred to as View Angle Tilting (VAT) that virtually eliminates mis-registration in the x-direction in a spin-echo sequence was proposed by Cho et al [8]. The VAT spin-echo sequence is identical to a CSE pulse sequence, except that the slice-select gradient is reapplied during data acquisition. The spins with differing frequencies are then not only shifted along the x-axis, but also along the slice-select (z-) axis. However, applying a gradient in the z-direction at the same time as along the x-direction has the effect of tilting the view angle, $\theta = \arctan(G_z / G_x)$, so the displacements in the x-direction and the z-direction cancel each other out (see Figure 3.1).

One disadvantage of VAT is that images are blurred in the read direction. In the original paper, this was explained to be a result of the tilted view angle θ , with the blurring expressed as a distance:

$$d = T \tan \theta = T \frac{G_{ss}}{G_r} \quad (3.18)$$

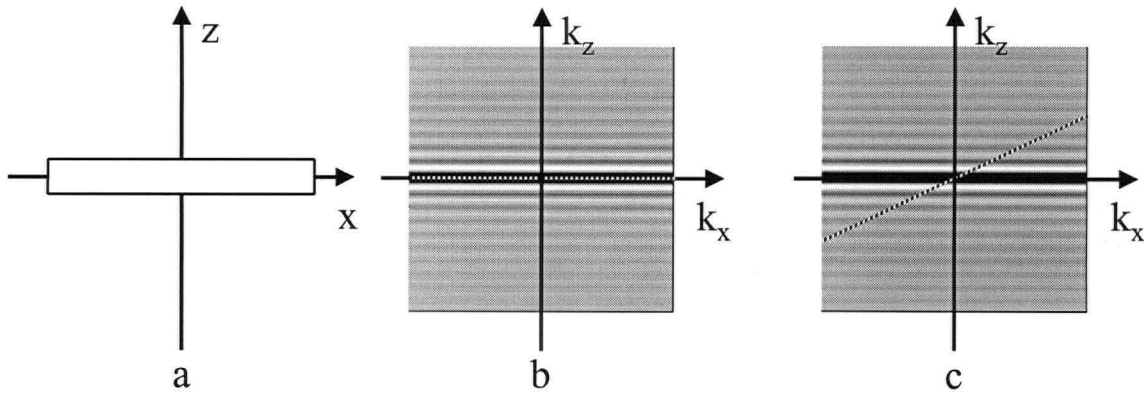


Figure 3.2: Oblique k-Space Sampling

The selected slice (a) and its k-space data sampled horizontally in an ordinary 2D sequence (b) and obliquely in a 2D sequence with VAT or “Z-Offset” (c). The k-space samples in (c) have smaller intensities for high spatial frequencies. This is equivalent to a blurring operator.

where T is the slice thickness. More recently, induction signal modulation by the slice-select gradient during frequency-encoding was suggested as another cause of blurring [29]. It can be better intuitively explained using 3D k-space, in which it becomes clear that the blur is a result of low-pass filtering. The k-space data is sampled horizontally in an ordinary sequence, but obliquely in a sequence with VAT. This reduces the intensities of high spatial frequencies, which is equivalent to a low-pass filter or blurring operator, as shown in Figure 3.2.

3.5 Z-Offset

An alternate way to intuitively explain how VAT works is referred to as “z-offset”. In a conventional spin-echo pulse sequence, during the slice-selective excitation all of the spins that are flipped are precessing at a frequency within a narrow band. Once the gradient is removed, they no longer experience the same magnetic field because of the inhomogeneity, and hence do not all possess the same Larmor frequency. To give the spins the same Larmor frequency during frequency-encoding, the same gradient used to select them is reapplied simultaneously with the read gradient [12]. The slice will not be perfectly flat, since there is no compensation in the z-direction, but the slice distortion is not nearly as significant as the effect in the x-direction. The z-offset theory is illustrated in Figure 3.3 and Figure 3.4.

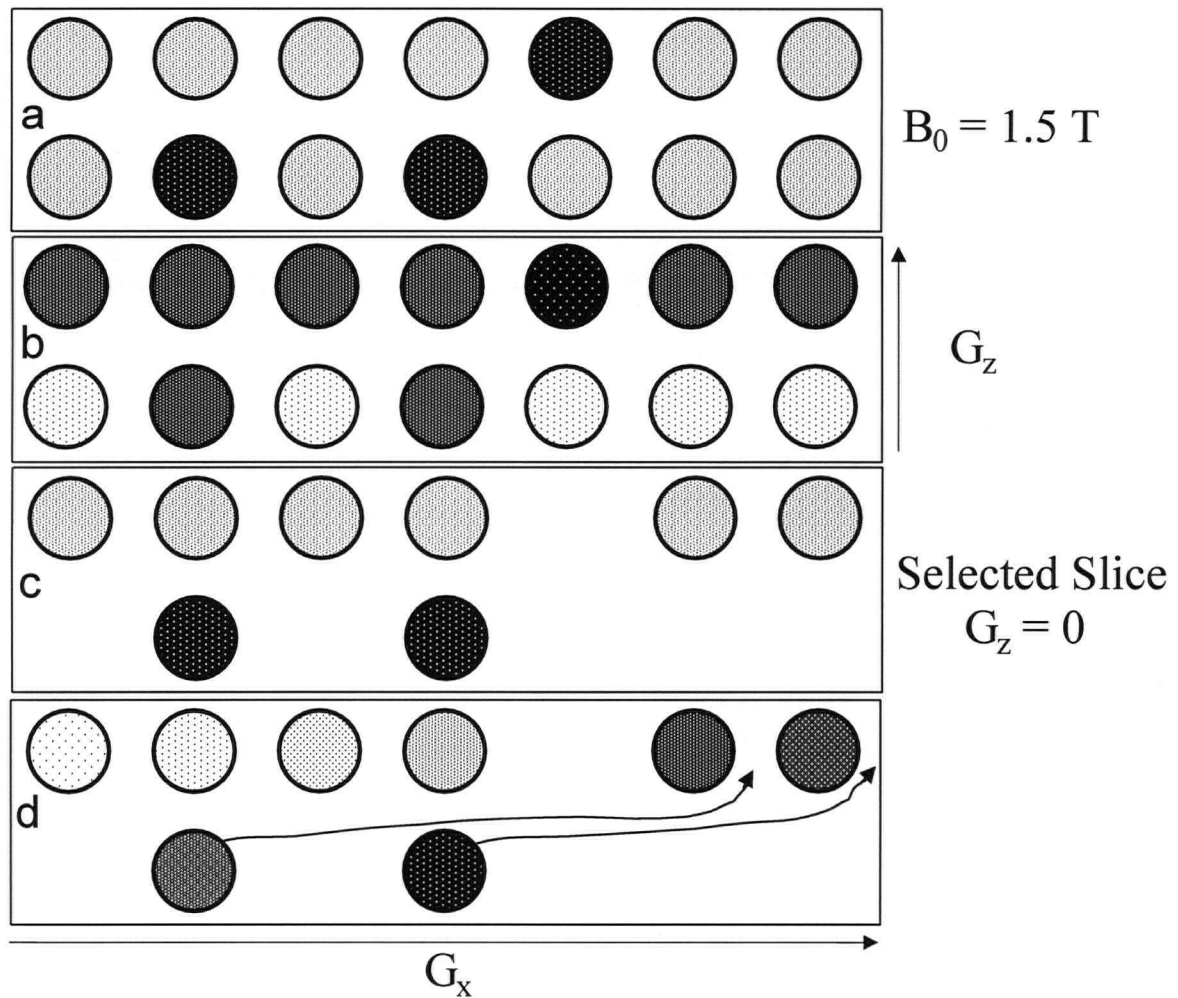


Figure 3.3: Illustration of Z-Offset Theory – No VAT applied

2 rows of spins. In (a), an external magnetic field of 1.5T is applied, but three of the spins experience a larger magnetic field due to susceptibility inhomogeneities (darker color). In (b), a slice-select gradient is applied in the z-direction, such that the spins in the top row are now experiencing a larger magnetic field, and those in the bottom row experience a smaller magnetic field. The three affected spins do not experience the prescribed magnetic field. In (c), the spins with the larger magnetic field are selected and flipped. Those that were not experiencing that magnetic field are not shown as they were not excited. The gradient is removed and the spins again experience the same magnetic field as they did in (a). In (d), the frequency-encoding gradient is applied, but the affected spins do not experience the prescribed magnetic field, and are mapped to the wrong spatial locations.

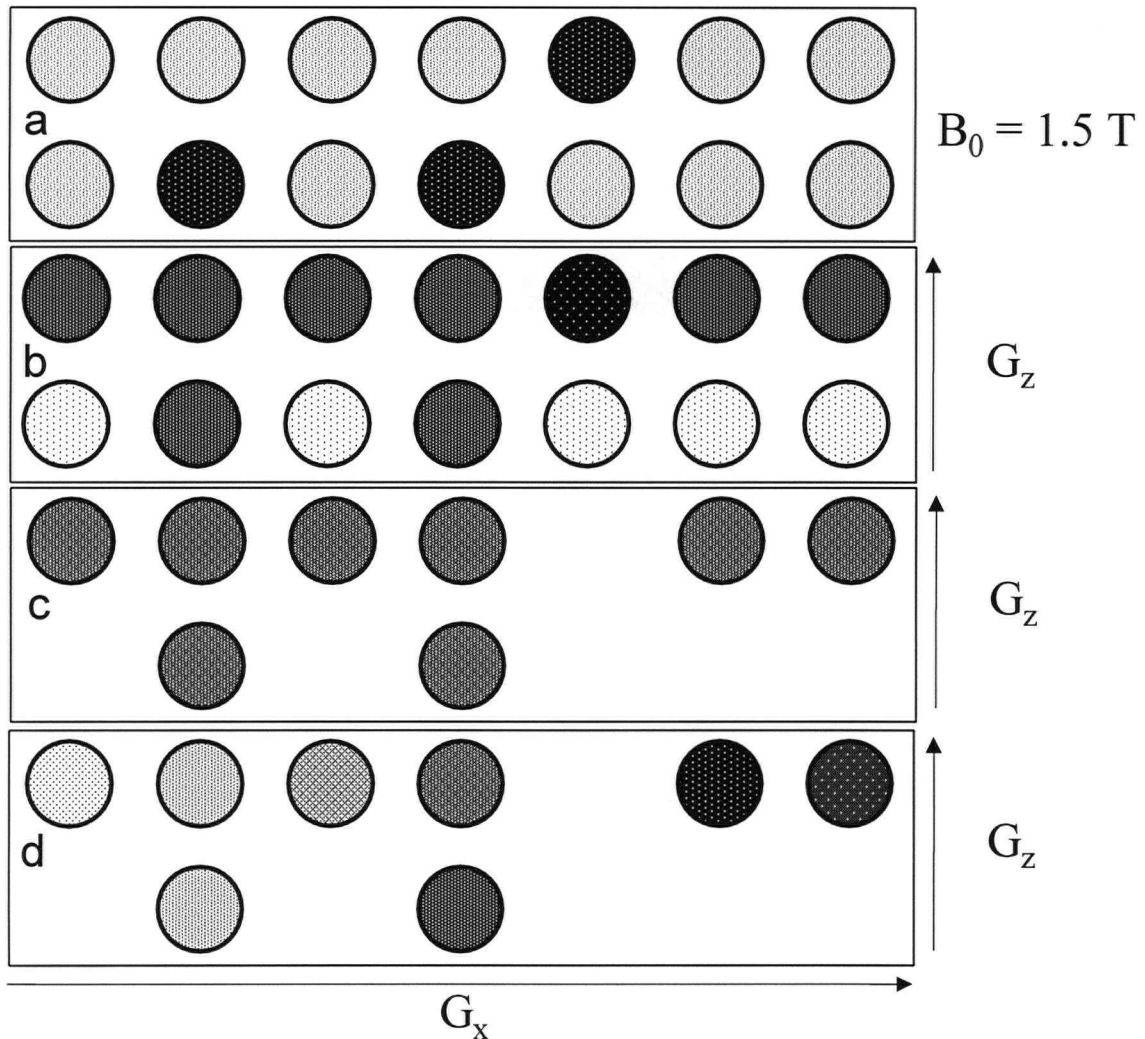


Figure 3.4: Illustration of Z-Offset Theory – VAT applied

(a) and (b) are the same as in Figure 3.3. In (c), VAT is applied, so the slice-select gradient is still applied after the excitation. Therefore all selected spins are experiencing the same magnetic field. In (d), the affected spins are not mis-mapped along the x-axis, so the magnetic susceptibility artifact is much reduced. The slice is still not flat, but this effect is not as severe.

The z-offset interpretation has several advantages over the original VAT explanation. It explains the need for the slice-select gradient to have the same direction and amplitude during its re-application as during its original application. According to the theory of VAT, it should not matter what G_z and G_x are, as long as their ratio gives the desired θ . The VAT interpretation also makes little sense when the k-space trajectory is complicated, while the z-offset model has no such limitations.

4 Materials and Methods

4.1 Introduction

In order to study the effectiveness of various metal artifact reduction techniques, it is necessary to create a “gold standard”, which demonstrates what an image of the subject would look like if it were free of metal artifact. Only then can the severity of the metal artifact be quantitatively measured and compared between imaging techniques. To this end, two types of phantoms were imaged; one contained a metal prosthesis immersed in water intended to produce severe metal artifact, and the other contained a wax replica of the metal prosthesis immersed in the same container of water, intended to produce an identical image, only free of metal artifact. Each phantom was imaged using a variety of metal artifact reduction techniques and the difference was determined between the images obtained from each phantom using the same pulse sequence. This chapter will provide an overview of the phantoms constructed and the MRI pulse sequences and parameters used. It will also describe the energy relationships analysis method, used to quantify the metal artifact, noise and blur in order to generate the results presented in chapter 5.

4.2 Phantom Design and Construction

Four different phantoms were imaged for the study of metal artifact reduction. Each phantom consisted of one of four femoral hip joint replacement prostheses suspended in the same 18 liter container filled with water. The properties of the phantom were changed by replacing the prosthesis. The first prosthesis was made of stainless steel (Thackray SD 548-13), the second was a wax replica of the stainless steel prosthesis, the third was made of titanium (titanium/chromium-cobalt - Zimmer 6032-09), and the fourth was a wax replica of the titanium prosthesis. Whichever prosthesis was being imaged at the time was held securely in place by three plastic stands designed such that the position of the prosthesis would always be the same, leaving no room for movement. It was further fixed in place using elastic bands. The phantom was positioned such that the orientation of the prosthesis was similar to how it would be positioned in vivo.

An image of one of the metal prostheses would contain severe metal artifact, while an image of its respective wax replica placed in the same container in the same position on the stands

would be identical, only free of any metal artifact. Wax was selected as the material for the replicas because its magnetic susceptibility is very similar to that of water, therefore it causes negligible susceptibility artifact.

The wax replicas were created by forming a two-part mold of the respective metal prosthesis from air-drying clay. A slab of clay approximately 2 cm thick and long and wide enough that the prosthesis, once placed in the middle, would have at least 2 cm between it and the edge of the clay, was lightly coated with talcum powder, and two strands of thread were laid across it widthwise. The prosthesis was pressed halfway into the clay such that the threads were between it and the clay to facilitate extraction. Mold keys were created by making dents in the clay far from the prosthesis so that once completed, the two halves would be easy to line up. A small cylinder was pressed into the clay to make a channel from the edge of the clay to the tip of the prosthesis to pour the wax through once completed. After leaving this half of the mold to dry overnight with the prosthesis and the cylinder still embedded in the clay, a similar slab of clay coated in talcum powder was pressed on top of the first. The clay was carefully massaged into all of the grooves and the mold keys. The mold was then left overnight. Once dry, the top half of the mold was gently removed. The cylinder was removed, and the prosthesis was pried out with the aid of the strands of thread. Both halves of the mold were once more coated in talcum powder and pressed together, using the mold keys to line them up. They were then bound with elastic bands. Candle wax was melted in a metal can placed in boiling water, then poured into the mold through the channel, and allowed to harden. The mold was gently pried apart, and the wax prosthesis was extracted by gently tapping on the clay. After trimming any excess wax, the replica was complete. Figure 4.1 is a photograph of the two metal prostheses and their wax replicas.

For analysis of the blurring caused by the different pulse sequences, a phantom manufactured by Picker International containing doped water, and featuring several vials and various structures including line pairs was used.

4.3 MRI Pulse Sequences and Imaging Parameters

An identical set of scans were performed on all of the phantoms, so that the image of the wax replica acted as a “gold standard”, containing the same signal but with negligible magnetic susceptibility artifact.

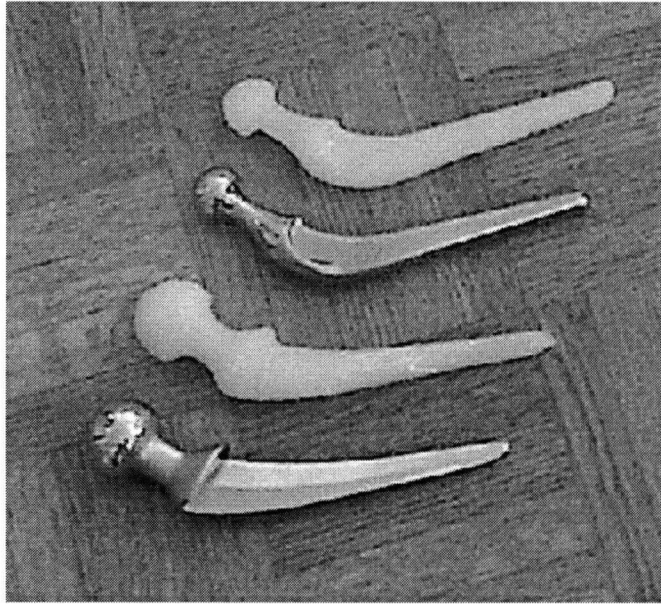


Figure 4.1: Metal and Wax Prostheses

From top to bottom: wax replica of stainless steel metal femoral hip joint replacement prosthesis, stainless steel prosthesis, wax replica of titanium prosthesis, titanium prosthesis.

After imaging the phantom containing the metal prosthesis, the phantom was removed from the scanner, the lid was removed from the container, and the metal prosthesis was replaced with its wax replica. The wax prosthesis was secured into exactly the position the metal prosthesis had just occupied. The lid was replaced and the table was advanced to the same spatial position it had occupied for the previous series of scans. Thus the images were already well aligned, and required no further registration. The difference between the images of the metal prosthesis and its wax replica yielded a measure of the artifact present in the image of the metal prosthesis.

A 1.5 T GE Signa MR scanner (General Electric Medical Systems, Milwaukee, WI) operating at the Epic 5.7 software level was used to obtain coronal images. The body coil was employed, and all scans used a TR of 550 msec and a TE of 24 msec. One average was taken. The FOV was 32 cm by 32 cm, and the slice thickness was 3 mm with no gaps. The matrix was 256 by 256, and the data was collected in two interleaved acquisitions.

Each phantom was scanned with a series of ten different pulse sequences, all with the above parameters. The first scan will be referred to as a “conventional” scan, using the default slice-select bandwidth of 886 Hz, and an image bandwidth (BW) of ± 15.63 kHz. The second

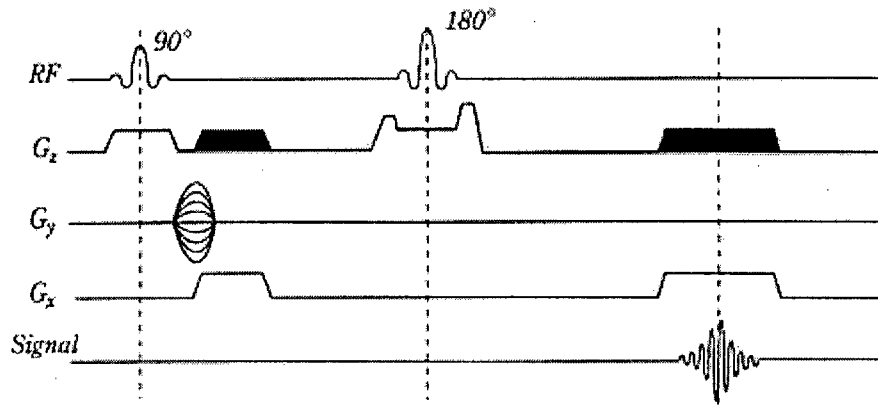


Figure 4.2: Timing Diagram for CSE Pulse Sequence Using VAT

The additional compensation gradient G_z (shaded areas) has a magnitude equal to the original slice-selection gradient, but is applied at the same time as the read gradient [8].

scan used the same image BW, but the slice-select bandwidth was increased by approximately 20%. Specifically, the amplitude of the slice-select gradient during the 180° pulse was multiplied by 1.2, and the amplitude of the slice-select gradient during the 90° pulse was set to the same value. Both pulse widths were divided by 1.2 to maintain a constant area. Unfortunately, the pulse widths were imperfect due to the limited resolution of the scanner. The relative RF levels were adjusted such that an area ratio of 1:2 was maintained between the 90° and 180° pulses. The third through seventh sequences all used the default slice-select bandwidth, but had varied image BWs. They were, respectively, ± 7.81 kHz, ± 12.5 kHz, ± 20.83 kHz, ± 31.2 kHz and ± 62.5 kHz. The eighth sequence used the default slice-select bandwidth, and an image BW of ± 15.63 kHz, but also included VAT. The VAT spin-echo pulse sequence is shown in Figure 4.2. The ninth sequence used the default slice-select bandwidth, but an image BW of ± 62.5 kHz, and VAT. The final sequence was the Metal Artifact Reduction Sequence (MARS), which includes the increased slice-select bandwidth (by 20%), an image BW of ± 62.5 kHz, and VAT.

For blur analysis, axial images were obtained of the phantom manufactured by Picker International containing doped water and featuring line pairs. The head coil was used with the same image parameters as above except the FOV was 24 x 24 cm. Six of the pulse sequences were used, namely, the conventional scan, the increased slice-select bandwidth, the image BW of ± 62.5 kHz, VAT, VAT with image BW ± 62.5 kHz, and MARS.

4.4 Analysis

4.4.1 Theory

The energy, E , of an MR image can be defined to be the sum of the squares of the voxel intensities of the image. The energy can be calculated in image space or in the reciprocal k -space, since it is conserved according to Parseval's theorem regarding energy conservation under Fourier Transform [30].

If the image is considered [31, 32] to consist of a noise field, N , superimposed on a noise-free signal field, S , its energy is calculated as

$$E = \sum_{\text{voxel}} (S + N)^2 \quad (4.1)$$

$$= \sum_{\text{voxel}} S^2 + \sum_{\text{voxel}} N^2 + 2 \sum_{\text{voxel}} SN. \quad (4.2)$$

If the noise is a zero-mean, uncorrelated random field, the last term can be neglected for a large number of voxels. If E_S and E_N are defined as the energy of the signal field and noise field respectively, then

$$E = E_S + E_N. \quad (4.3)$$

Note that for a magnitude image, the distribution of noise is different in the background of the image where the signal is zero than where the signal is much larger than the noise. The noise superimposed on the signal can be taken to be normally distributed, with zero mean and standard deviation equal to that of the channel noise [32]. In the background, the noise is Rayleigh distributed due to the modulus operation. For the following calculations, it is assumed that the noise is calculated from the region containing signal.

If the same phantom is scanned repeatedly, the signal field should remain the same while the noise field will vary. If the image resulting from one scan is subtracted from another, the total energy of the resultant difference image is

$$E_{\text{diff}} = \sum_{\text{voxel}} [(S + N_1) - (S + N_2)]^2 \quad (4.4)$$

$$E_{\text{diff}} = \sum_{\text{voxel}} N_1^2 + \sum_{\text{voxel}} N_2^2 - 2 \sum_{\text{voxel}} N_1 N_2. \quad (4.5)$$

The last term can be neglected as above, so the total difference energy is

$$E_{\text{diff}} = E_{N_1} + E_{N_2}. \quad (4.6)$$

If an image contains metal artifact, it can be considered to be another additive field, in this case an artifact field, A , superimposed on the signal field. Then the energy is given by

$$E = \sum_{\text{voxel}} (S + N + A)^2 \quad (4.7)$$

$$E = \sum_{\text{voxel}} S^2 + \sum_{\text{voxel}} N^2 + \sum_{\text{voxel}} A^2 + 2 \sum_{\text{voxel}} AS + 2 \sum_{\text{voxel}} NA + 2 \sum_{\text{voxel}} NS. \quad (4.8)$$

As above, the last two terms can be neglected. The cross terms involving A and S can also be neglected if the artifact field is assumed to be uncorrelated to the signal field and have a zero-mean. In the case of metal artifact, A does indeed have a zero mean because the nature of the metal artifact is such that voxel values are simply mapped to the wrong spatial location, so that no signal is gained or lost. Wherever signal is increased, it is decreased elsewhere, resulting in zero net change in signal.

If E_A is the energy of the artifact field, then

$$E = E_S + E_N + E_A. \quad (4.9)$$

While the above equation is a statistical approximation, a similar relationship has been shown empirically to be remarkably robust [33].

If one image is obtained by scanning a phantom consisting of water surrounding a metal prosthesis, and a second image is obtained of water surrounding a non-metallic replica of the metal prosthesis, using the same parameters, the signal fields should still be identical (provided RF tuning is the same), but the noise will be different, and only the first image will contain metal artifact. The total energy of the difference image is then

$$E_{\text{diff}} = \sum_{\text{voxel}} [(S + N_1 + A) - (S + N_2)]^2 \quad (4.10)$$

$$E_{\text{diff}} = \sum_{\text{voxel}} N_1^2 + \sum_{\text{voxel}} A^2 + \sum_{\text{voxel}} N_2^2 + 2 \sum_{\text{voxel}} N_1 A - 2 \sum_{\text{voxel}} N_1 N_2 - 2 \sum_{\text{voxel}} N_2 A \quad (4.11)$$

The last three terms can again be neglected, so the total difference energy is

$$E_{\text{diff}} = E_{N_1} + E_{N_2} + E_A. \quad (4.12)$$

If the sum of the squares of the voxel values in the difference image is calculated for an ROI known to contain no metal artifact (far from the prosthesis), it will be equal to the sum of the noise energies of the individual images ($E_N = E_{N_1} + E_{N_2}$). The total difference energy can be

obtained by summing the squares of the voxel values over the entire image ($E_{total} = E_{N_1} + E_{N_2} + E_A$). Both of these energies need to be normalized by dividing by the number of voxels involved in the calculation, and then E_A can be obtained by subtracting the former from the latter. This results in a quantitative measure of the artifact present in the image, E_A .

When calculating the noise energy, the signal may not be uniform across the image, so it is often calculated from the background of the image where there is no signal (only air). In this case, the Rayleigh distribution $P(n)$ of the noise leads to an expectation value for the sum square of the voxels of:

$$\langle E_{na} \rangle \propto \langle n_1^2 \rangle + \langle n_2^2 \rangle - 2\langle n_1 n_2 \rangle \quad (4.13)$$

$$\langle n_1^2 \rangle = \langle n_2^2 \rangle = \frac{\int_0^{\infty} P_1(n) n^2 dn}{\int_0^{\infty} P_1(n) dn} = \frac{\int_0^{\infty} n^3 \exp(-\frac{n^2}{2\sigma^2}) dn}{\int_0^{\infty} n \exp(-\frac{n^2}{2\sigma^2}) dn} = 2\sigma^2 \quad (4.14)$$

$$\begin{aligned} -2\langle n_1 n_2 \rangle &= -2 \frac{\int_0^{\infty} \int_0^{\infty} P_1(n_1) n_1 P_2(n_2) n_2 dn_1 dn_2}{\int_0^{\infty} \int_0^{\infty} P_1(n_1) P_2(n_2) dn_1 dn_2} \\ &= \frac{\int_0^{\infty} \int_0^{\infty} n_1^2 n_2^2 \exp(-\frac{n_1^2 + n_2^2}{2\sigma^2}) dn_1 dn_2}{\int_0^{\infty} \int_0^{\infty} n_1 n_2 \exp(-\frac{n_1^2 + n_2^2}{2\sigma^2}) dn_1 dn_2} \\ &= -\pi\sigma^2 \end{aligned} \quad (4.15)$$

where n_1 and n_2 are Rayleigh distributed random variables, and σ is the standard deviation of the channel noise. Thus

$$\langle E_{na} \rangle \propto 4\sigma^2 - \pi\sigma^2 \quad (4.16)$$

for the noise in the background. For the noise superimposed on the signal, which has a normal distribution $P(m)$,

$$\langle E_{ns} \rangle \propto \langle m_1^2 \rangle + \langle m_2^2 \rangle - 2\langle m_1 m_2 \rangle \quad (4.17)$$

$$\langle m_1^2 \rangle = \langle m_2^2 \rangle = \frac{\int_{-\infty}^{\infty} P_1(m) m^2 dm}{\int_{-\infty}^{\infty} P_1(m) dm} = \frac{\int_{-\infty}^{\infty} m^2 \exp(-\frac{m^2}{2\sigma^2}) dm}{\int_{-\infty}^{\infty} \exp(-\frac{m^2}{2\sigma^2}) dm} = \sigma^2 \quad (4.18)$$

$$\begin{aligned} -2\langle m_1 m_2 \rangle &= -2 \frac{\int_{-\infty}^{\infty} \int_{-\infty}^{\infty} P_1(m_1) m_1 P_2(m_2) m_2 dm_1 dm_2}{\int_{-\infty}^{\infty} \int_{-\infty}^{\infty} P_1(m_1) P_2(m_2) dm_1 dm_2} \\ &= \frac{\int_{-\infty}^{\infty} \int_{-\infty}^{\infty} m_1^2 m_2^2 \exp(-\frac{m_1^2 + m_2^2}{2\sigma^2}) dm_1 dm_2}{\int_{-\infty}^{\infty} \int_{-\infty}^{\infty} m_1 m_2 \exp(-\frac{m_1^2 + m_2^2}{2\sigma^2}) dm_1 dm_2} = 0 \end{aligned} \quad (4.19)$$

where m_1 and m_2 are normally distributed, so

$$\langle E_{ns} \rangle \propto 2\sigma^2. \quad (4.20)$$

Thus the noise energy as measured from air must be multiplied by a factor of $1/(2-\pi/2)$ in order to correct for the modulus operation in creating a magnitude image [27].

The blur was treated separately, and analyzed in the same manner by replacing the artifact field A with a blur field, Bl. The blur field is uncorrelated and has a zero-mean. If an object is imaged first with a conventional pulse sequence, and then with a sequence anticipated to produce blur (Bl) as well as other artifacts (A), the two images can be subtracted to produce a difference image, with energy

$$E_{diff} = \sum_{voxel} [(S + N_1) - (S + N_2 + Bl + A)]^2 \quad (4.21)$$

$$E_{diff} = \sum_{voxel} N_1^2 + \sum_{voxel} N_2^2 + \sum_{voxel} Bl^2 + \sum_{voxel} A^2 \quad (4.22)$$

$$E_{diff} = E_{N_1} + E_{N_2} + E_B + E_A. \quad (4.23)$$

All cross terms were neglected since N_1 , N_2 , A, and Bl are uncorrelated zero-mean fields. The noise can be isolated using one of the methods outlined above, and E_A can be isolated by using images not expected to produce blur. Subtracting the contributions from noise and other artifact yields a measure of the blur present in the image, E_B .

A more general analysis can be executed using the "gradient energy" [33], which is similar to the above energy, only summing the squares of the partial derivatives of the voxels with

respect to the x-axis. Using partial derivatives insures that the additive fields are "noise like", i.e. uncorrelated and having zero-mean. The gradient energy must be used when comparing two randomly selected clinical images, in which case the sum of the energies of the two images is not equal to the energy of the difference image, but the sum of the gradient energies is equal to the gradient energy of the difference image [33]. The derivative operator has the effect of accentuating edges, which are the most affected by blur. The gradient energy analysis for blur would be performed as follows.

The gradient energy can be defined as:

$$Eg = \sum_{\text{voxel}} \left(\frac{\partial S}{\partial x} \right)^2, \quad (4.24)$$

where x is considered to be the frequency-encoding direction. If an object is imaged using a conventional pulse sequence, and then again with a pulse sequence expected to produce blur (Bl) as well as other artifacts (A), and the gradients of the two images along the frequency-encoding direction are subtracted to yield a gradient difference image, its gradient energy will be defined as

$$Eg_{diff} = \sum_{\text{voxel}} \left[\left(\frac{\partial S}{\partial x} + \frac{\partial N_1}{\partial x} \right) - \left(\frac{\partial S}{\partial x} + \frac{\partial N_2}{\partial x} + \frac{\partial B}{\partial x} + \frac{\partial A}{\partial x} \right) \right]^2 \quad (4.25)$$

$$Eg_{diff} = \sum_{\text{voxel}} \left(\frac{\partial N_1}{\partial x} \right)^2 + \sum_{\text{voxel}} \left(\frac{\partial N_2}{\partial x} \right)^2 + \sum_{\text{voxel}} \left(\frac{\partial B}{\partial x} \right)^2 + \sum_{\text{voxel}} \left(\frac{\partial A}{\partial x} \right)^2 \quad (4.26)$$

$$Eg_{diff} = Eg_{N_1} + Eg_{N_2} + Eg_B + Eg_A. \quad (4.27)$$

All cross terms can be neglected since the derivative operator produces uncorrelated zero-mean fields. The noise can be isolated as above, and Eg_A can be isolated by contrasting images obtained by comparing pulse sequences expected to differ only in terms of artifact other than blur. Subtracting the contributions from noise and other artifact yields a measure of the blur present in the image, Eg_B .

In this work, all of the superimposed fields (N, A, Bl) had the inherent property of being uncorrelated and having zero-means. The gradient energy approach was not reported in this study because the results using the gradients did not yield appreciably different results, and it is less intuitive.

4.4.2 Implementation

Image analysis was performed using PV Wave software (Visual Numerics). The signal intensities were first normalized by dividing by the mean signal intensity obtained from various ROIs far from the prosthesis because the different pulse sequences produced different signal levels. This is attributed to RF effects caused by the prosthesis de-tuning the coil. The image of the phantom containing the wax prosthesis was then subtracted from that of the phantom containing the respective metal prosthesis, resulting in a difference image, which represents the difference from what would be expected for a metal artifact free image. The sum of the squares of the resulting pixels (the total energy) was divided by the total number of voxels summed over to obtain a measure of the normalized total energy between the image with artifact and that without. This discrepancy was caused by a combination of noise and artifact.

The noise contribution, E_N , was isolated by performing the same analysis in the background of the image, where there was no signal. Therefore the energy was simply the sum of the noise energies of the two individual images. The Rayleigh distributed noise in air had to be converted to the parent normal distribution expected for the water signal, so the noise energy was divided by $(2-\pi/2)$ [27].

Subtracting the noise contribution from the total difference between the images produced a measure of the artifact, E_A .

An assessment of the blur was obtained by imaging the phantom containing doped water and line pairs (Picker International) with a CSE pulse sequence with an image BW of ± 15.63 kHz, and with each of the artifact reduction pulse sequences, as above. An ROI was selected containing only the line pairs. The normalized image obtained with the conventional pulse sequence was subtracted from the normalized results from each of the other techniques, and the total energy was calculated. The noise energy was isolated as described for the metal artifact analysis. Subtracting the contribution from noise and other sources associated with changing bandwidths yielded a measure of the blur energy for the pulse sequences that used VAT.

5 Results

5.1 Introduction

As detailed in section 4.3, different pulse sequences were used on the same phantom in order to quantify the effectiveness of the underlying metal artifact reduction techniques.

The severity of metal artifact can be lessened by increasing the frequency-encoding bandwidth. In the image, the artifact takes the form of mis-mapped signal, because there is a change in precession frequency induced by the metal that is not purposefully prescribed by the pulse sequence. When the image BW is increased, the magnitude of the image distortion is reduced because the BW per pixel is increased, decreasing the extent of mis-registration in the frequency-encoding direction. The effects of increasing and decreasing the image BW were investigated.

The shift along the slice-select direction can be similarly reduced by increasing the bandwidth along the slice-select axis. In slice-selection, metal artifact takes two forms: distortion of the location of the slice, and distortion of its width. Increasing the slice-select bandwidth decreases the relative difference in Larmor frequencies, which then decreases the size of the transfer along the slice-select direction, resulting in a slice that is less warped. The effectiveness of this technique was studied by changing the slice-select bandwidth in conjunction with other image parameters.

Another factor that was changed in order to determine its effect on metal artifact was the type of metal. Materials with larger magnetic susceptibilities such as stainless steel or cobalt chrome cause more metal artifact than titanium alloys, making titanium the more MR compatible metal. Therefore magnetic susceptibility has become one of the most important factors considered in selecting the type of metal used for a prosthesis, along with the more traditional considerations such as cost, availability and mechanical qualities. To determine the significance of this factor, both stainless steel and titanium/chromium-cobalt prostheses were examined.

Finally, the effectiveness of VAT was investigated. VAT addresses the problem of the spins no longer experiencing the same magnetic field because of the inhomogeneity caused by the presence of the metal after the slice-select gradient is removed, and hence not all possessing the same Larmor frequency. To give the spins the same Larmor frequency during frequency-

encoding, the same gradient used to select them is reapplied simultaneously with the read gradient. VAT was applied in combination with other metal artifact reduction techniques.

Some techniques to minimize the susceptibility artifact were not easily altered, and were therefore used consistently for all of the scans.

In particular, the alignment of the metal component is important. Since both components were paramagnetic, they were aligned parallel to the direction of \mathbf{B}_0 in order to minimize interactions with the magnetic field. Paramagnetic materials have positive magnetic susceptibilities, meaning that the spins align with \mathbf{B}_0 . This is not the case for diamagnetic materials, such as bismuth, antimony, sodium chloride, gold, or mercury, which have negative magnetic susceptibilities. The spins in diamagnetic substances align at right angles to the external magnetic field; therefore interactions with the magnetic field would be minimized if it were positioned perpendicular to \mathbf{B}_0 . In this study, it was also beneficial to position the metal component parallel to \mathbf{B}_0 since that was also the direction in which it would be positioned in a clinical situation.

The frequency-encoding axis was also aligned with the long axis of the metal component. The mis-mapping of signal takes place primarily along the frequency-encoding direction, so the least amount of signal from the water (or in a clinical situation, tissue) will be affected if the shortest axis of the component is orthogonal to the frequency-encoding axis. It was also advantageous from a data processing point of view, since it minimized the number of voxels that were physically located inside the prosthesis but were mapped to a region in the water, and vice-versa, minimizing the energy.

The body coil was used since the RF tuning of larger coils is less affected by the presence of metal, and also because it would be used in vivo.

Instead of a gradient-echo sequence, a spin-echo sequence was used, which employs a 180° refocusing pulse, minimizing signal loss due to spin dephasing.

In this chapter, both qualitative and quantitative results are presented. The qualitative results consist of images obtained of each of the phantoms using each of the pulse sequences, and the differences in the images are discussed. The quantitative results are the outcome of the energy calculations, providing measures of the metal artifact, noise and blur. The findings are discussed and compared to expectations.

5.2 Qualitative Results - Images

A single coronal slice through the center of the phantom containing the stainless steel prosthesis is shown in Figure 5.1 imaged with each of the pulse sequences used as follows: (a) a conventional spin-echo pulse sequence with image BW ± 15.63 kHz, (b) increased slice-select bandwidth (by 20%) with image BW ± 15.63 kHz, (c) default slice-select bandwidth with image BW ± 7.81 kHz, (d) default slice-select bandwidth with image BW ± 12.5 kHz, (e) default slice-select bandwidth with image BW ± 20.83 kHz, (f) default slice-select bandwidth with image BW ± 31.2 kHz, (g) default slice-select bandwidth with image BW ± 62.5 kHz, (h) default slice-select bandwidth with image BW ± 15.63 kHz and VAT, (i) default slice-select bandwidth with image BW ± 62.5 kHz and VAT, (j) MARS: increased slice-select bandwidth with image BW ± 62.5 kHz and VAT, (k) MARS with 10 averages, and (l) a photograph of the phantom.

It can be seen qualitatively that smaller image BWs result in more metal artifact, and the prosthesis is barely recognizable in (a), (c), and (d). Increasing the slice-select bandwidth alone has very little effect, as seen in (b). Increasing the image BW reduces the metal artifact, but also the SNR, as seen in (e), (f), and (g). Applying VAT has an enormous effect, as seen by comparing (h) and (a), which differ only in the application of VAT. Increasing the image BW as well as applying VAT further reduces the metal artifact, but also the SNR, as seen in (i). (j) appears to have the least amount of metal artifact overall, indicating the qualitative success of the MARS sequence. With additional averages (k), the image obtained using MARS is clearly the most distinct image.

Figure 5.2 shows the phantom containing the wax replica of the stainless steel prosthesis imaged with each of the respective pulse sequences as listed for Figure 5.1, except the MARS using additional averages. It can be seen by comparing the respective images to their counterparts in Figure 5.1 that the scans involving VAT are much closer to the "gold standard" of the wax-replica. From these images, the difference in SNR between the pulse sequences is more obvious since there is no metal artifact to obscure the effect.

Figure 5.3 and Figure 5.4 show the phantoms containing the titanium prosthesis and its wax replica imaged with each of the respective pulse sequences as listed above, showing similar results.



Figure 5.1: Qualitative Results – Steel Prosthesis

The phantom containing the stainless steel prosthesis imaged with (a) a conventional spin-echo pulse sequence with image BW ± 15.63 kHz, (b) increased slice-select bandwidth with image BW ± 15.63 kHz, (c) default slice-select bandwidth with image BW ± 7.81 kHz, (d) default slice-select bandwidth with image BW ± 12.5 kHz, (e) default slice-select bandwidth with image BW ± 20.83 kHz, (f) default slice-select bandwidth with image BW ± 31.2 kHz, (g) default slice-select bandwidth with image BW ± 62.5 kHz, (h) default slice-select bandwidth with image BW ± 15.63 kHz and VAT, (i) default slice-select bandwidth with image BW ± 62.5 kHz and VAT, (j) MARS: increased slice-select bandwidth with image BW ± 62.5 kHz and VAT, (k) MARS with 10 averages, and (l) a photograph of the phantom.

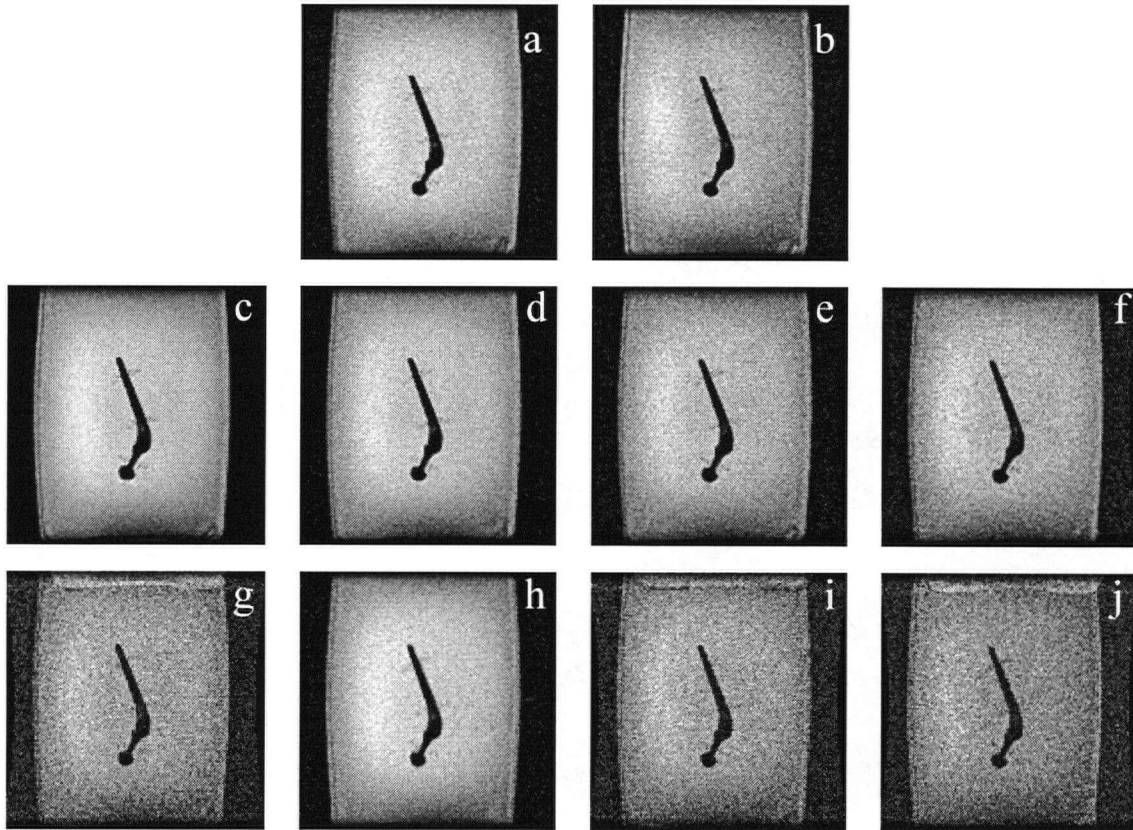


Figure 5.2: *Qualitative Results – Wax Replica of Steel Prosthesis*

The phantom containing the wax replica of the stainless steel prosthesis imaged with (a) a conventional spin-echo pulse sequence with image BW ± 15.63 kHz, (b) increased slice-select bandwidth with image BW ± 15.63 kHz, (c) default slice-select bandwidth with image BW ± 7.81 kHz, (d) default slice-select bandwidth with image BW ± 12.5 kHz, (e) default slice-select bandwidth with image BW ± 20.83 kHz, (f) default slice-select bandwidth with image BW ± 31.2 kHz, (g) default slice-select bandwidth with image BW ± 62.5 kHz, (h) default slice-select bandwidth with image BW ± 15.63 kHz and VAT, (i) default slice-select bandwidth with image BW ± 62.5 kHz and VAT, and (j) MARS: increased slice-select bandwidth with image BW ± 62.5 kHz and VAT.



Figure 5.3: Qualitative Results – Titanium Prosthesis

The phantom containing the titanium prosthesis imaged with (a) a conventional spin-echo pulse sequence with image BW ± 15.63 kHz, (b) increased slice-select bandwidth with image BW ± 15.63 kHz, (c) default slice-select bandwidth with image BW ± 7.81 kHz, (d) default slice-select bandwidth with image BW ± 12.5 kHz, (e) default slice-select bandwidth with image BW ± 20.83 kHz, (f) default slice-select bandwidth with image BW ± 31.2 kHz, (g) default slice-select bandwidth with image BW ± 62.5 kHz, (h) default slice-select bandwidth with image BW ± 15.63 kHz and VAT, (i) default slice-select bandwidth with image BW ± 62.5 kHz and VAT, (j) MARS: increased slice-select bandwidth with image BW ± 62.5 kHz and VAT, (k) MARS with 10 averages, and (l) a photograph of the phantom.

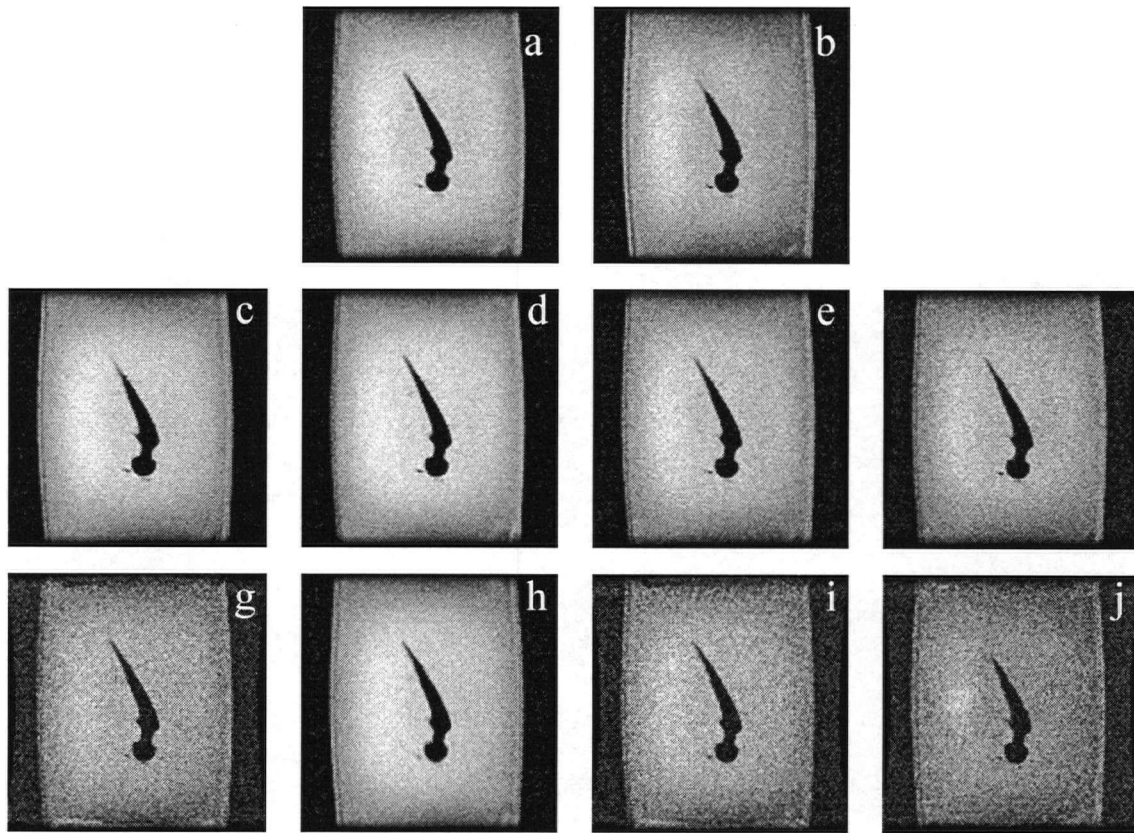


Figure 5.4: Qualitative Results – Wax Replica of Titanium Prosthesis

The phantom containing the wax replica of the titanium prosthesis imaged with (a) a conventional spin-echo pulse sequence with image BW ± 15.63 kHz, (b) increased slice-select bandwidth with image BW ± 15.63 kHz, (c) default slice-select bandwidth with image BW ± 7.81 kHz, (d) default slice-select bandwidth with image BW ± 12.5 kHz, (e) default slice-select bandwidth with image BW ± 20.83 kHz, (f) default slice-select bandwidth with image BW ± 31.2 kHz, (g) default slice-select bandwidth with image BW ± 62.5 kHz, (h) default slice-select bandwidth with image BW ± 15.63 kHz and VAT, (i) default slice-select bandwidth with image BW ± 62.5 kHz and VAT, and (j) MARS: increased slice-select bandwidth with image BW ± 62.5 kHz and VAT.

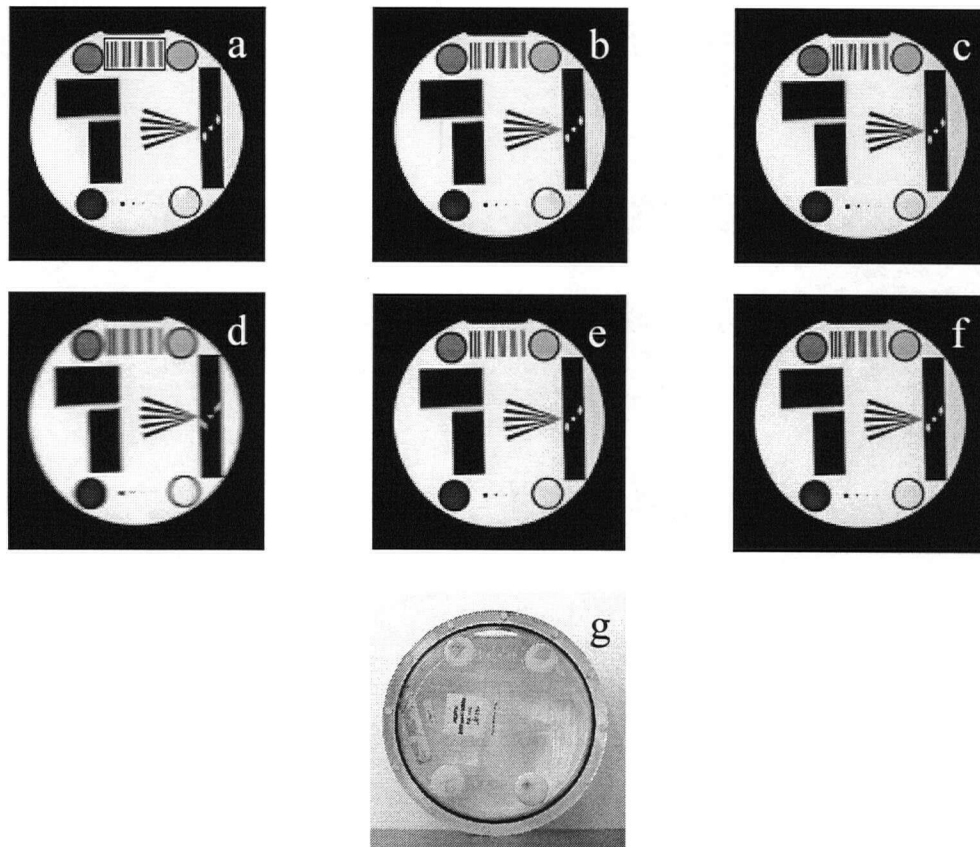


Figure 5.5: Qualitative Results – Picker International Phantom

The Picker International phantom imaged with (a) a CSE pulse sequence, (b) an increased slice-select bandwidth (which had a negligible difference compared to the CSE pulse sequence), (c) an increased image BW of ± 62.5 kHz, (d) VAT (which has substantial blurring), (e) VAT compared with an increased image BW of ± 62.5 kHz, and (f) MARS. (g) is a photograph of the phantom.

Figure 5.5 shows the Picker International phantom imaged with (a) a conventional spin-echo pulse sequence with image BW ± 15.63 kHz, (b) increased slice-select bandwidth with image BW ± 15.63 kHz, (c) default slice-select bandwidth with image BW ± 62.5 kHz, (d) default slice-select bandwidth with image BW ± 15.63 kHz and VAT, (e) default slice-select bandwidth with image BW ± 62.5 kHz and VAT, (f) MARS: increased slice-select bandwidth with image BW ± 62.5 kHz and VAT, and (g) a photograph of the phantom. The ROI used to analyze blur is illustrated in (a) as a rectangle enclosing the vertical lines. It can be seen by comparing (a) and (d) that the application of VAT greatly blurs the line pairs, rendering the well defined edges inside the ROI in (a) much less distinct. The increased image BW used in conjunction with VAT in (e) and (f) greatly reduces the haziness of the line pairs, making

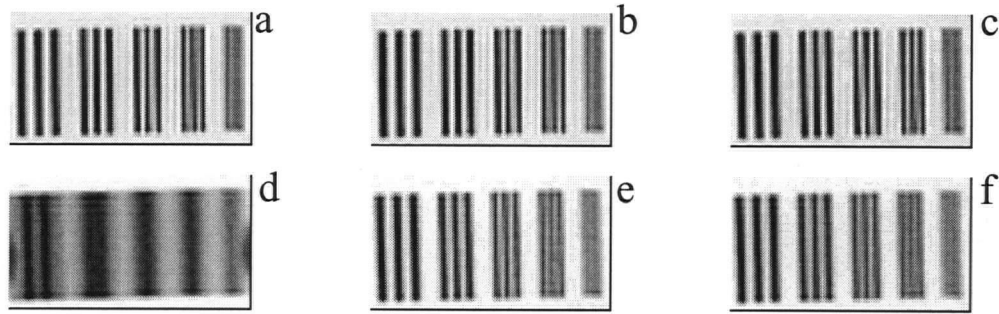


Figure 5.6: *Qualitative Results – ROI used in Picker International Phantom*
 ROI selected from the Picker International phantom imaged with (a) a CSE pulse sequence, (b) an increased slice-select bandwidth, (c) an increased image BW of ± 62.5 kHz, (d) VAT, (e) VAT with an increased image BW of ± 62.5 kHz, and (f) MARS.

them much sharper, although still not as sharp as for the CSE sequence. A magnification of the ROI used for analysis is shown for the respective pulse sequences in Figure 5.6.

5.3 Quantitative Results - Energy

The quantitative results are the outcome of the energy calculations as outlined in section 4.4. All images were first normalized by dividing by an average intensity value found in regions far from any metal artifact in order to account for any differences in tuning. The energy is defined as the sum of the square of the voxel values for a specific region, and all energy values were normalized by dividing by the total number of voxels in that region.

5.3.1 Metal Artifact

The metal artifact was analyzed by subtracting the image of the wax prosthesis from the corresponding image of the respective metal prosthesis using the same pulse sequence (after normalizing), then summing the squares of the voxel values and dividing by the number of voxels. This was summed over all slices to yield the total difference energy. ROIs were selected in the background of the image, and the sum of the squares of these voxels was divided by the number of voxels in the ROI. The noise energy was obtained by dividing these numbers by $(2-\pi/2)$ [27] to account for the difference in noise distributions in air and water. Since both images were obtained using the same pulse sequence, and there were very few edges in the phantom, blur artifact was assumed to be negligible. Thus subtracting the

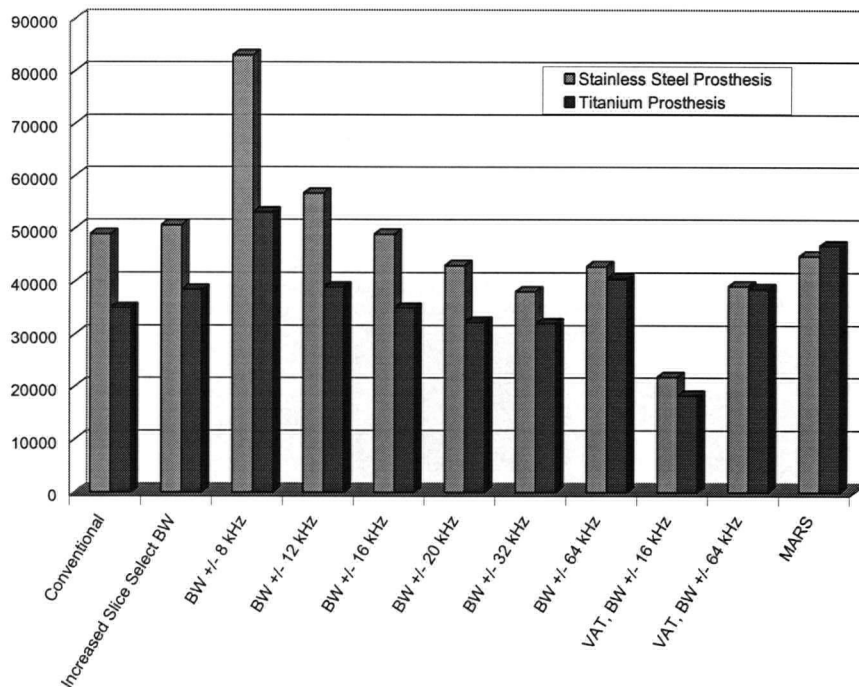


Figure 5.7: Total Energy for Various Metal Artifact Reduction Techniques

The first sequence was a “conventional” scan, using an image bandwidth of ± 15.63 kHz. The second sequence used the same image BW, but the slice-select bandwidth was increased by 20%. The third through eighth sequences used image BW’s of ± 7.81 kHz, ± 12.5 kHz, ± 15.63 kHz, ± 20.83 kHz, ± 31.2 kHz and ± 62.5 kHz, respectively. The ninth sequence used an image BW of ± 15.63 kHz, but also included VAT. The tenth sequence used an image BW of ± 62.5 kHz as well as VAT. The final sequence was MARS, which includes the increased slice-select bandwidth (by 20%), an image BW of ± 62.5 kHz, and VAT.

noise energy from the total energy provided the metal artifact energy, directly related to the amount of metal artifact in the image.

5.3.1.1 Total Difference Energy

The total difference energy is shown in Figure 5.7 for the steel and titanium prostheses for several pulse sequences. The first sequence was a “conventional” scan, using an image BW of ± 15.63 kHz. The second sequence used the same image BW, but the slice-select bandwidth was increased by 20%. The third through eighth sequences used image BW’s of ± 7.81 kHz, ± 12.5 kHz, ± 15.63 kHz, ± 20.83 kHz, ± 31.2 kHz and ± 62.5 kHz, respectively.

The ninth sequence used an image BW of ± 15.63 kHz, but also included VAT. The tenth sequence used an image BW of ± 62.5 kHz as well as VAT. The final sequence was MARS, which includes the increased slice-select bandwidth (by 20%), an image BW of ± 62.5 kHz, and VAT. It is interesting that the images produced by each pulse sequence, each representing a different metal artifact reduction technique or a combination of several, yielded a fairly consistent value for total difference energy. The only two cases that differed significantly were the scan with an image BW of ± 7.81 kHz, which had 52% more total difference energy than the conventional scan in the case of the titanium prosthesis and 69% more energy in the case of the stainless steel prostheses, and the pulse sequence using VAT which had 48% and 55% less total difference energy respectively. The total difference energy encompasses both noise and artifact, so it is necessary to break it into its component values in order to truly evaluate the techniques.

5.3.1.2 Noise Energy

The contribution of the noise to the total energy for each artifact reduction technique is seen in Figure 5.8 for each of the aforementioned pulse sequence using each of the stainless steel and titanium prostheses. As predicted by section 2.6, the square of the noise was proportional to the image bandwidth. In fact, this relationship held true to within 4%, except in the case of the image BW of ± 7.81 kHz which was higher than expected, possibly because the noise was so low it was nearing the lower limit for the system. This relationship provides great validation to the analysis technique.

The noise energy was larger when the slice-select bandwidth was increased. This was likely due to non-optimal pulse widths, which caused a loss of signal. Since the noise energy is actually a measure of the noise-to-signal ratio, less signal results in a larger noise energy. The noise was the highest for the MARS sequence because it used both an increased image BW and suffered imperfections introduced by the addition of the increased slice-select bandwidth. The noise energy was quite insensitive to the application of VAT, giving a great advantage to this method of reducing metal artifact.

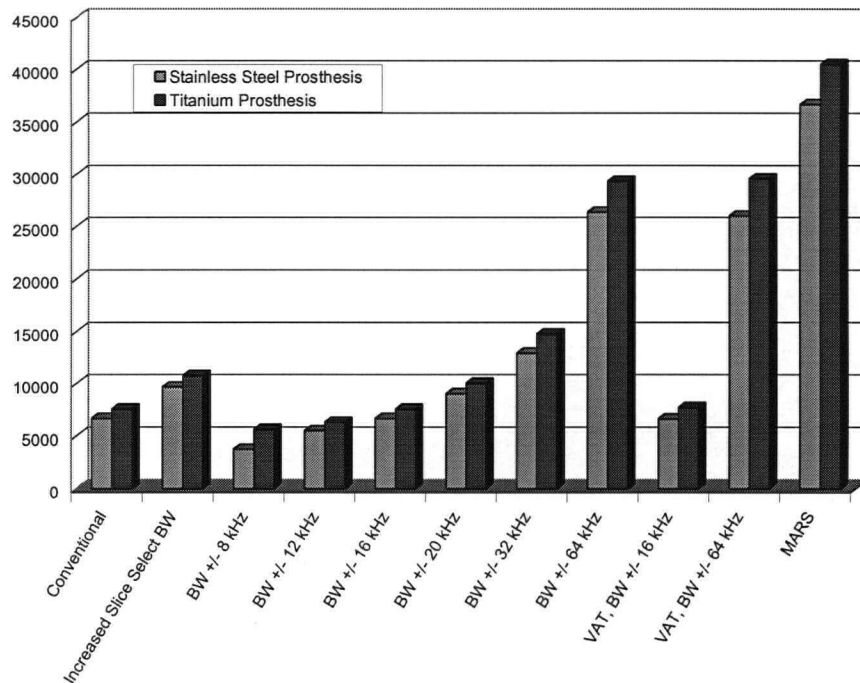


Figure 5.8: Noise Contribution to Total Energy

Noise energy for the results of all of the artifact reduction techniques. The noise energy was proportional to the square of the image bandwidth, but was relatively insensitive to the application of VAT.

5.3.1.3 Artifact Energy

The artifact energy was obtained by subtracting the noise energy from the total difference energy. The quantification of the artifact could be considered to be the most important result, as noise can be reduced by taking multiple averages. The results for the various pulse sequences described above for both metal prostheses can be seen in Figure 5.9.

The artifact energy results revealed that the titanium prosthesis induced less metal artifact than the stainless steel prosthesis (on average, 33% less). This is consistent with expectations based on the magnetic susceptibility of the prostheses. Thus in terms of MRI compatibility, a titanium prosthesis is preferable to a stainless steel prosthesis.

Increasing the slice-select bandwidth did not have a great effect on the metal artifact energy. This was anticipated since the increase in slice-select bandwidth was implemented to ease the distortion in the slice-select direction, which tends to be much less significant than the artifact in the frequency-encoding direction.

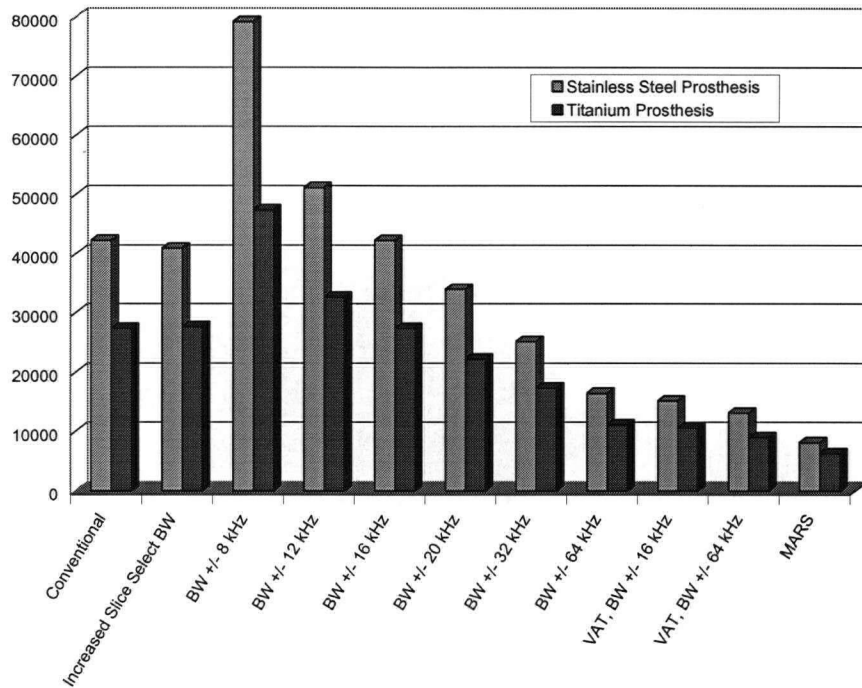


Figure 5.9: Artifact Energy

A relative measurement of the amount of artifact present in an image obtained with each of the metal artifact reduction techniques. The artifact was lowered slightly when the slice-select bandwidth was increased. The scan with an image BW of ± 7.81 kHz had between 73% and 87% more artifact than the conventional scan for the titanium and stainless steel prostheses respectively, and the scan with an image BW of ± 12.5 kHz had on average 20% more artifact. Increasing the image BW decreased the artifact by an average of 19% for an image BW of ± 20.83 kHz, 39% for an image BW of ± 32.5 kHz, and 60% for an image BW of ± 62.5 kHz. VAT alone reduced the artifact by an average of 63%, combining VAT with a larger bandwidth reduced it by 68%, and adding a larger slice-select bandwidth (MARS) reduced it by 79% on average.

Decreasing the image bandwidth increased the metal artifact, as predicted. For an image bandwidth of ± 7.81 kHz, in comparison to the CSE scan, the artifact energy was 73% higher for the titanium prosthesis and 87% higher for the stainless steel prosthesis. For an image BW of ± 12.5 kHz, the artifact energy was 19% higher for the titanium prosthesis, and 21% higher for the stainless steel prosthesis.

Accordingly, increasing the image bandwidth decreased the metal artifact. The scan with an image BW of ± 20.83 kHz had 19% less artifact than that of the CSE scan for both metal prostheses, the scan with an image BW of ± 31.2 kHz had 37% less artifact energy for the

titanium prosthesis and 40% less for the stainless steel prosthesis, and the scan with an image BW of ± 62.5 kHz had 59% and 61% less artifact energy, respectively.

Simply applying VAT without altering the image BW had an even greater effect than even increasing the image BW to ± 62.5 kHz. For the titanium prosthesis, it had 61% less metal artifact than the conventional scan, and for the stainless steel prosthesis, it had 64% less. The metal artifact was further reduced by applying VAT as well as increasing the image BW to ± 62.5 kHz, with 67% and 69% less metal artifact than the conventional scan for the titanium and stainless steel prostheses, respectively. But the greatest artifact reduction was accomplished by the MARS sequence. The metal artifact energy using the MARS sequence was 77% lower than using the CSE sequence for the titanium prosthesis, and 81% lower for the stainless steel prosthesis.

So, although using VAT alone without increasing the image BW produced the lowest total difference energy, MARS produced the lowest metal artifact energy. As the higher total energy given by the MARS sequence was mostly due to the contribution from noise, the image obtained with MARS had the lowest amount of artifact. The noise can be reduced by taking additional averages.

5.3.2 Blur

The phantoms used to quantify metal artifact were not optimal for measuring blur because they consisted of mainly water, expected to give a uniform signal. Blurring is only apparent along edges and boundaries, so a phantom containing sharp boundaries was required. To this end, a phantom manufactured by Picker International containing doped water and line pairs was used, with the line pairs acting as a standard with which blurring could be quantified. In this case, the "gold standard" containing no blur could not be accomplished by changing the phantom. Instead, the pulse sequence was changed. Only pulse sequences employing VAT were expected to produce blur, so the identical pulse sequence without VAT was used as the gold standard. The images resulting from each pulse sequence were subtracted from the image resulting from a CSE scan, and the total difference energy and the noise energy were obtained as for the metal artifact analysis. After subtracting the noise energy from the total difference energy, the total artifact energy remained, encompassing any artifact that differed between that particular pulse sequence and the CSE pulse sequence. The blur energy was

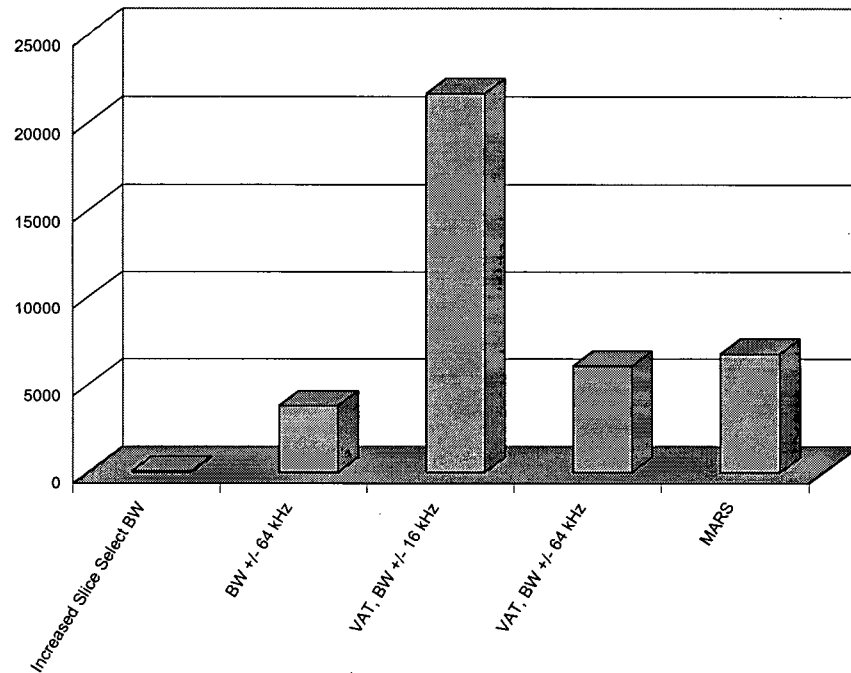


Figure 5.10: Total Energy for Blur Study

Total difference energy for blur study for five different pulse sequences in comparison to the results from a conventional spin-echo pulse sequence. The pulse sequences used were an increased slice-select bandwidth (which had a negligible difference compared to the CSE pulse sequence), an increased image BW of ± 62.5 kHz, VAT, VAT with an increased image BW of ± 62.5 kHz, and MARS. The VAT pulse sequence had the greatest total difference energy compared to the CSE pulse sequence.

obtained for the pulse sequences using VAT by subtracting the total artifact energy for an identical pulse sequence not using VAT from its total artifact energy. Because a different phantom was used, the scale is consistent within the blur results (section 5.3.2) but is not relevant to the scale used for the metal artifact results (section 5.3.1).

5.3.2.1 Total Difference Energy

Figure 5.10 shows the total difference energy obtained by summing the square of the voxel values for voxels inside the ROI outlined in Figure 5.5a after subtracting the results from the conventional spin-echo pulse sequence. The pulse sequences used were increased slice-select bandwidth with image BW ± 15.63 kHz, default slice-select bandwidth with image BW ± 62.5 kHz, default slice-select bandwidth with image BW ± 15.63 kHz and VAT, default

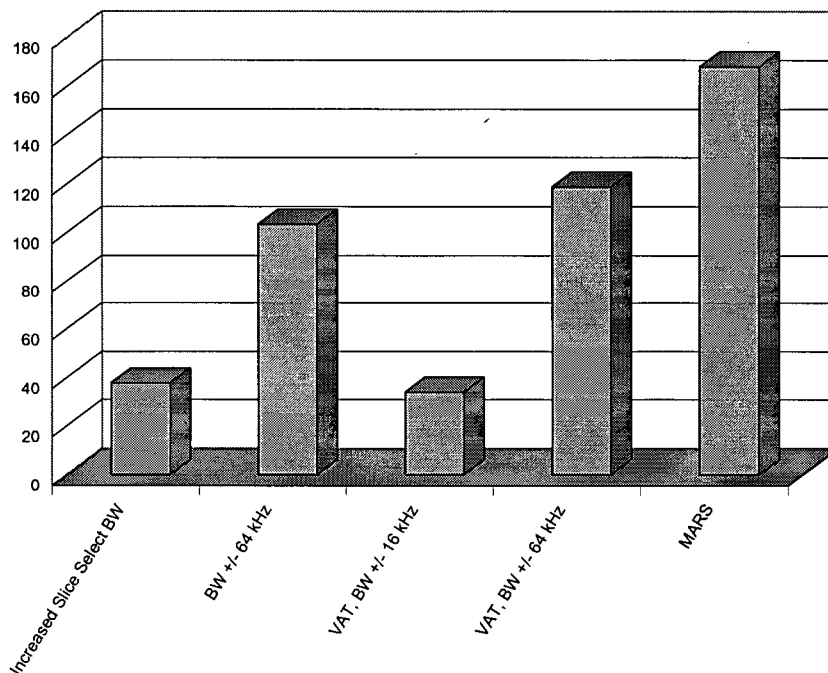


Figure 5.11: Noise Energy for Blur Study

The noise was the greatest for the results of the MARS pulse sequence, as in the metal artifact study.

slice-select bandwidth with image BW ± 62.5 kHz and VAT, and MARS: increased slice-select bandwidth with image BW ± 62.5 kHz and VAT. There is nearly no difference between the images resulting from the CSE pulse sequence and that with increased slice-select bandwidth, and a large difference for the sequence using VAT alone.

5.3.2.2 Noise Energy

The noise energy was obtained using the background signal, and the multiplication factor to compensate for the different noise distribution in air and water was used, exactly as for the metal artifact analysis above. The results are seen in Figure 5.11. The relative noise energy levels are consistent with those obtained for the metal artifact analysis, with the increased slice-select bandwidth generating slightly more noise than VAT alone, and the increased image BW resulting in much higher noise energy.

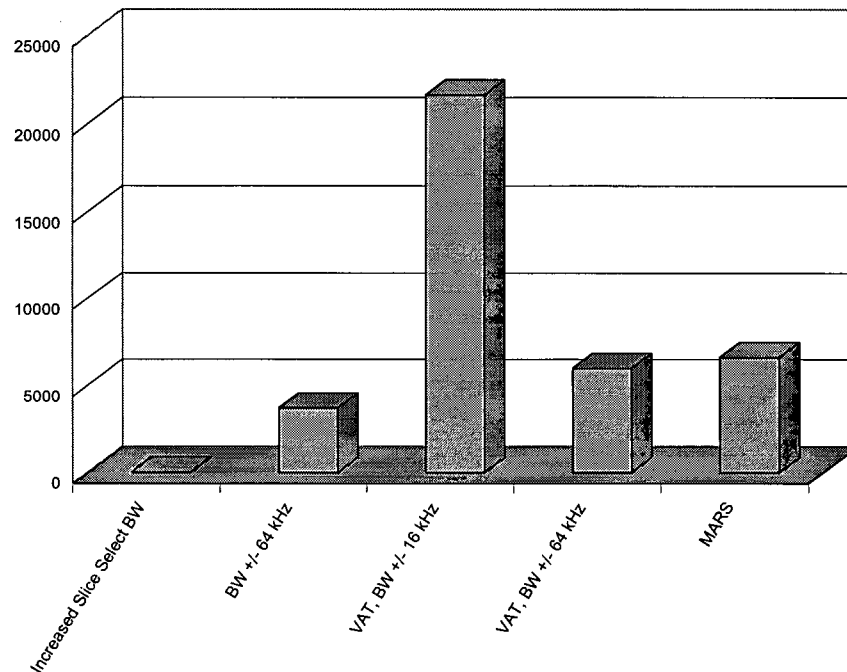


Figure 5.12: Total Artifact Energy for Blur Study

The artifact could stem from the different image bandwidths, slice-select bandwidth, or slice thicknesses.

5.3.2.3 Total Artifact Energy

Differences between the images could result not only from blur, but also from other factors introduced by changing the pulse sequence. For instance, changing the image BW changes the magnitude of any susceptibility artifact, and changing the slice-select bandwidth may slightly change the slice thickness due to limited resolution. The total artifact energy results, obtained by subtracting the noise energy from the total difference energy, are seen in Figure 5.12. For the increased slice-select bandwidth, the total artifact energy is negligible, implying that the slice thickness remained quite uniform. For the increased image BW, the total artifact energy is significant, indicating that there is a significant change in susceptibility artifact between the CSE pulse sequence and the increased image BW. The three pulse sequences employing VAT must be further broken down into blur and other artifact for the final conclusion.

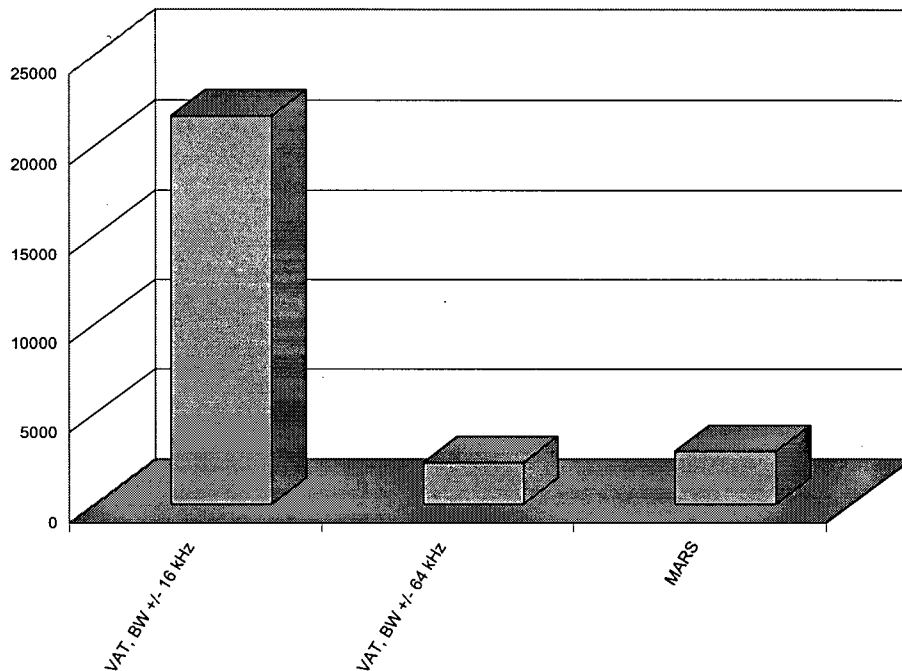


Figure 5.13: Blur Energy for Artifact Reduction Techniques Involving VAT

The blur was found to be greatly reduced by increasing the image bandwidth, and slightly increased by increasing the slice-select bandwidth.

5.3.2.4 Blur Energy

In order to study the blur caused by pulse sequences using VAT, the artifact energy from other causes had to be removed. Thus the total artifact energy resulting from a sequence that was identical except for the application of VAT was subtracted from the total artifact energy of the images created using sequences employing VAT.

The sequence using an image BW of ± 15.63 kHz and VAT was the same as the conventional sequence except for the use of VAT, so the only artifact should be blurring, so the total artifact energy needed no further manipulation. The sequence using VAT and an image BW of ± 62.5 kHz differed from the CSE pulse sequence in the change in image BW as well as the application of VAT, so the total artifact energy of the sequence using an image BW of ± 62.5 kHz (without VAT) was subtracted. Finally, the MARS sequence differed from the CSE sequence in the application of VAT, the increase in image BW, and the increase in slice-select BW, so the total artifact energy from the sequence using an image BW of ± 62.5 kHz,

and that of the sequence using an increased slice-select BW, were subtracted. The results can be seen for the three pulse sequences including VAT in Figure 5.13.

The MARS sequence produced much less blur (87% less) than VAT alone, a fantastic improvement. The pulse sequence using VAT and the increased image BW (± 62.5 kHz) had even less blur (89% less than VAT alone), indicating that the increase in the slice-select bandwidth actually increased the blurring slightly. These results are quite consistent with Equation (3.18), which indicates that the blur is expected to be proportional to the slice thickness, the gradient in the slice-select direction, and the inverse of the frequency-encoding gradient. Since the blur energy is the square of the blur, and gradients are proportional to bandwidths, it should be proportional to the square of the slice thickness, the square of the slice-select bandwidth, and the inverse square of the image BW. Using Equation (3.18), the expected decrease in blur using the MARS pulse sequence over VAT alone was 91%, and using VAT plus an image BW of ± 62.5 kHz was 93%. The 4% discrepancy could be partly attributed to changing slice thicknesses, or induction signal modulation.

6 Conclusions

6.1 Quantitative Analysis of Metal Artifact

A new method of obtaining quantitative measurements of metal artifact was proposed and implemented. This “gold standard” method of creating a non-metallic replica of a metallic prosthesis and imaging both with the same MR pulse sequence was simple and easy to implement. The analysis, involving energy relationships, was not computationally intensive. The results for the noise energy matched predictions and served to validate both the “gold standard” imaging method and the analysis technique. Thus the investigation of metal artifact need no longer be limited to the more traditional qualitative studies.

6.2 Metal Artifact Reduction

Phantoms containing stainless steel or titanium prostheses or their wax replicas were imaged using several different pulse sequences, altering the image bandwidth and the slice-select bandwidth, and with and without VAT (View Angle Tilting). By comparing the images obtained of the metallic phantom to the image obtained of the wax replica using the same pulse sequence, the noise and metal artifact could be separated and quantified. The noise energy followed expected trends, depending directly on the image bandwidth. The metal artifact decreased significantly with increasing image bandwidth, and decreased slightly with increased slice-select bandwidth. VAT dramatically reduced metal artifact. The most metal artifact reduction was accomplished with the MARS pulse sequence, which combined VAT with increased image bandwidth and increased slice-select bandwidth, but it also produced the lowest SNR of the sequences tested.

6.3 Blur

The blur artifact was measured for the pulse sequences involving VAT using the line pairs in a Picker International phantom. The blur was found to be severe using VAT alone, but was greatly reduced using the MARS pulse sequence. Thus even though the MARS pulse sequence had a poor SNR, its vast superiority in terms of blur reduction and metal artifact reduction recommend it as an extremely valuable tool in imaging patients with metal prostheses.

6.4 Future Work

The method proposed for quantifying metal artifact can be easily applied to study other metal artifact reduction techniques, and create a catalog of metal artifact reduction techniques and their respective efficiencies. It could also be used to separate metal artifact into susceptibility artifact and conductivity artifact by creating a replica out of a non-conducting substance with a similar susceptibility to the metal object. In fact, it could be extended to study many other types of artifact.

The obvious success of VAT as a metal artifact reduction technique suggests that further work to improve or extend the versatility of pulse sequences employing it would be valuable both to research and clinical imaging. MARS has been shown to be a large improvement over simply applying VAT to a conventional spin-echo pulse sequence by dramatically reducing the blurring, encouraging further attempts to include VAT in pulse sequences. For instance, VAT could be implemented in a fast spin-echo (FSE) or echo-planar imaging (EPI) pulse sequence.

Bibliography

- [1] Olsen RV, Munk PL, Lee MJ, Janzen DL, MacKay AL, Xiang Q-S, Masri B. Metal Artifact Reduction Sequence: Early Clinical Applications. *Radiographics* 2000;20:699-712.
- [2] Wood, Michael. Artifact identification and elimination. *RSNA Categorical Course in Physics: The Basic Physics of MR Imaging* 1997; 59-69.
- [3] Patola W, Coulter B. MRI Artifacts.
<http://www1.stpaulshosp.bc.ca/stpaulsstuff/MRart/cs.html>. Last accessed August 22, 2003.
- [4] Czervionke LF, Daniels DL, Wehrli FW, Mark LP, Hendrix LE, Strandt JA, Williams AL, Haughton VM. Magnetic susceptibility artifacts in gradient-recalled echo MR imaging. *AJNR* 1988;9:1149-1155.
- [5] Laakman RW, Kaufman B, Han JS, Nelson AD, Clampitt M, O'Block AM, Haaga JR, Alfidi RJ. MR imaging in patients with metallic implants. *Radiology* 1985;157:711-714.
- [6] Petersilge CA, Lewin JS, Duerk JL, Yoo JU, Ghaneyem AJ. Optimizing imaging parameters for MR evaluation of the spine with titanium pedicle screws. *AJR* 1996;166:1213-1218.
- [7] Eustace S, Goldberg R, Williamson D, Melhem ER, Oladipo O, Yucel EK, Jara H. MR imaging of soft tissues adjacent to orthopaedic hardware: techniques to minimize susceptibility artefact. *Clin Radiol* 1997; 52:589-594.
- [8] Cho ZH, Kim DJ, Kim YK. Total inhomogeneity correction including chemical shifts and susceptibility by view angle tilting. *Med Phys* 1988;15:7-11.

- [9] McGowan AJ, MacKay AL, Xiang Q-S, Connel DG, Janzen DL, Munk PL. Reduction of image distortion in the presence of metal. In: Proceeding of the 5th Annual Meeting ISMRM, Vancouver, British Columbia, Canada, 1997. p 1973.
- [10] Chang SD, Lee MJ, Munk PL, Janzen DL, MacKay A, Xiang Q-S. MRI of spinal hardware: Comparison of conventional T1-weighted sequence with a new metal artifact reduction sequence. *Skeletal Radiol* 2001;30:213-218.
- [11] Butts K, Pauly JM, Daniel BL, Kee S, Norbash AM. Management of biopsy needle artifacts: Techniques for RF-refocused MRI. *JMRI* 1999;9:586-595.
- [12] Lee MJ, Janzen DL, Munk PL, MacKay A, Xiang Q-S, McGowan A. Quantitative assessment of an MR technique for reducing metal artifact: application to spin-echo imaging in a phantom. *Skeletal Radiol* 2001;30:398-401.
- [13] Rabi II, Zacharias JR, Millman S, Kusch P. A new method of measuring nuclear magnetic moment. *Phys Rev* 1938;53:318.
- [14] Rabi II, Millman S, Kusch P, Zacharias JR. The Molecular Beam Resonance Method for Measuring Nuclear Magnetic Moments The Magnetic Moments of ${}^6_3\text{Li}$, ${}^7_3\text{Li}$ and ${}^{19}_9\text{F}$. *Phys Rev* 1939;55:526-535.
- [15] Bloch F, Hansen WW, Packard M. Nuclear Induction. *Phys Rev* 1946;69:127.
- [16] Bloch F. Nuclear Induction. *Phys Rev* 1946;70:460-474.
- [17] Purcell EM, Torrey HC, Pound RV. Resonance absorption by nuclear magnetic moments in a solid. *Phys Rev* 1946;69:37-38.

- [18] Ernst RR, Anderson WA. Application of Fourier transform spectroscopy to magnetic resonance. *Rev Sci Instrum* 1966;37:93-102.
- [19] Lauterbur PC. Image formation by induced local interactions: examples employing nuclear magnetic resonance. *Nature* 1973;242:190-191.
- [20] Krane KS. *Introductory Nuclear Physics*. John Wiley & Sons Publishing, New York. 1987.
- [21] Hashemi RH, Bradley WG. *MRI: The Basics*. Williams and Wilkins, Philadelphia. 1997.
- [22] Mazziotta JC, Gilman S. *Clinical Brain Imaging: Principles and Applications*. F. A. Davis Co., Philadelphia. 1992.
- [23] Slichter CP. *Principles of Magnetic Resonance*. Springer-Verlag, New York, 3rd Edition. 1990.
- [24] Hahn EL. Spin echoes. *Phys Rev* 1950;80:580-594.
- [25] Carr HY, Purcell EM. Effects of diffusion on free precession in nuclear magnetic resonance experiments. *Phys Rev* 1954;94:630-638.
- [26] Meiboom S, Gill D. Modified spin echo method for measuring relaxation times. *Rev Sci Instrum* 1958;29:688-691.
- [27] Edelstein WA, Bottomley PA, Pfeifer LM. A signal-to-noise calibration procedure for NMR imaging systems. *Med Phys* 1984;11:180-185.
- [28] Lai C-M. Reconstructing NMR images from projections under inhomogeneous magnetic field and non-linear field gradients. *Phys Med Biol* 1983;28:925-938.

- [29] Butts K, Pauly JM. Reduction of blurring in view angle tilting MRI. In: Proceeding of the 10th Annual Meeting ISMRM, Honolulu, Hawaii, USA, 2002. p 382.
- [30] Bracewell RN. The Fourier Transform and its applicaions, 3rd ed. New York: McGraw-Hill; 1999.
- [31] Xiang Q-S. Optimal k-space averaging for efficient noise reduction. In: Proceeding of the 10th Annual Meeting ISMRM, Honolulu, Hawaii, USA, 2002. p 2435.
- [32] Brummer ME, Mersereau RM, Eisner RL, Lewine RRJ. Automatic Detection of Brain Contours in MRI Data Sets. IEEE Trans Med Imaging 1993;12:153-166.
- [33] Xiang Q-S, Bronskill MJ, Henkelman RM. Two-point interference method for suppression of ghost artifact due to motion. JMRI 1993;3:900-906.